Department of Precision and Microsystems Engineering

Non-linear Stiffness Estimation using Two-Tone Excitation

Marc Krijgsman

Report no : 2025.069
Coach : Ir. C.F.D. Wattjes, Prof. Dr. P.G. Steeneken
Professor : Dr. F. Alijani
Specialisation : HTE-ED
Type of report : Master Thesis
Date : 22 October 2025

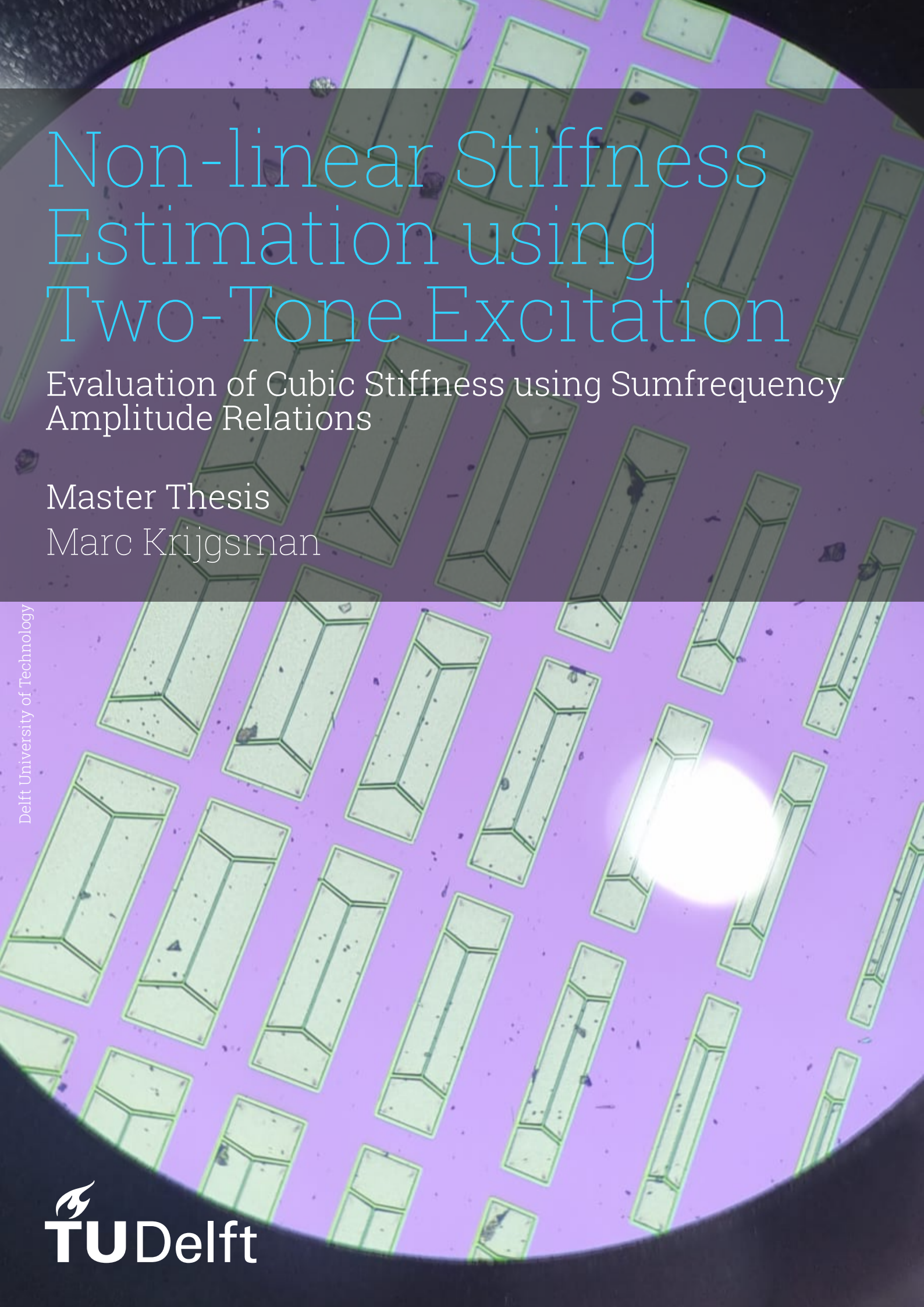

Non-linear Stiffness Estimation using Two-Tone Excitation

Evaluation of Cubic Stiffness using Sumfrequency Amplitude Relations

Master Thesis

Marc Krijgsman

Delft University of Technology

TU Delft

Non-linear Stiffness Estimation using Two-Tone Excitation

Evaluation of Cubic Stiffness using Sumfrequency Amplitude Relations

by

Marc Krijgsman

to obtain the degree of Master of Science
at the Delft University of Technology,
to be defended publicly on 2025 at AM.

Student number:	5013704	
Project duration:	August, 2024 – August, 2025	
Thesis committee:	Dr. F. Alijani,	supervisor
	Prof. dr. P. G. Steeneken,	supervisor
	Ir. C. Wattjes	daily supervisor

This thesis is confidential and cannot be made public until December 31, 2025.

Cover: Clamped nano-beams through a microscope, Marc Krijgsman

An electronic version of this thesis is available at `http://repository.tudelft.nl/`.

TU Delft

Summary

This thesis studies how to estimate cubic non-linear stiffness in dynamic systems using two-tone excitation. When a structure with cubic stiffness is driven at two frequencies that lie close to each other, it produces intermodulation peaks at sum and difference frequencies. By relating the amplitudes at these frequencies to the system parameters, the cubic stiffness can in principle be extracted without full-scale numerical modelling or fits with convoluted functions. An analytic relation between the amplitude at an excitation tone (A_1) and the first-order sumfrequency amplitude (A_3) is derived using the harmonic balancing method, expressed in terms of the resonance frequency ω_0, detuning δ, and cubic stiffness γ. The derivation uses a Ansatz with the corresponding sumfrequencies and orders terms to obtain a analytic relation. This analytic curve is then validated in two ways: (i) by numerically solving the harmonic-balance equations, and (ii) by direct time-domain integration (RK45) with amplitude extraction at the relevant frequencies. Symbolic regression is also used to fit compact additional formulas where the analytic relation loses accuracy. Experiments are carried out on Silicon-Nitride beams using a Polytec MSA-500 LDV and a Moku:Lab for signal generation and spectrum analysis.

The main result is that the analytic A_1–A_3 relation agrees well with harmonic-balance and numeric integration simulations, but only within a certain region: low to moderate drive and sufficiently separated tones so that higher-order products remain small. Outside this region, solution branching and neglected terms reduce accuracy. In measurements, the expected near-linear relation between the two drive amplitudes (A_1, A_2) is observed, but the measured A_1–A_3 curves rise more steeply than predicted. This could be caused by additional effects such as higher-order non-linearities, damping, or resonance shifts under strong drive.

The work delivers: (1) an analytic and numerical framework that maps where two-tone intermodulation can identify cubic stiffness, and (2) a robust experimental workflow. It also outlines future improvements: adding (non-linear) damping and quadratic stiffness to the model, lock-in based detection, better input conditioning, and resonance tracking to improve the differences between theory and experiments.

Contents

Summary i

Nomenclature iv

1 Introduction 1

2 Theory 2
2.1 Origin of Non-linearities in Microsystems . . . 2
2.2 Mathematical modelling of a dynamic system . . . 4
2.3 Two tone excitation response of a dynamic system . . . 5
2.4 Estimation of non-linear parameters using the Harmonic Balancing method . . . 6
2.4.1 Sumfrequency amplitude estimation by Harmonic Balancing . . . 7
2.4.2 Analytically Relating Sumfrequency Amplitudes to Excitation Amplitudes and system parameters . . . 9

3 Methodology 13
3.1 Research Question . . . 13
3.1.1 Sub-questions . . . 13
3.1.2 Research Goals . . . 14

4 Experimental Set-up 15
4.1 Overview of the Setup . . . 15
4.2 Non-linearities in the input signals due to components set-up . . . 17
4.2.1 Non-linearity in the Input Signal due to the Power Combiner . . . 17

5 Results 20
5.1 Comparing the Analytic Solution to Numerical Solutions . . . 20
5.1.1 Comparing the Analytic Solution to Numerical Solutions of the HB-equations . . . 20
5.1.2 Symbolic Regression of Numerical Solutions of HB-equations as Aid and Comparison . . . 23
5.1.3 Comparing the Analytic Solution to Solutions found by Numeric Integration Methods 31
5.2 Intermodulation Peaks from Experimental Measurements . . . 34
5.2.1 Influence of Sample Geometry and Measurement Location . . . 34
5.3 Validation of Analytic Relations with Experimental Data . . . 37
5.3.1 Non-linear Cubic Stiffness Estimation . . . 37

6 Conclusion 40

7 Discussion 42
7.1 Theory . . . 42
7.2 Experiments . . . 43
7.3 Recommendations for Future Work . . . 43

8 Acknowledgements 45

References 46

A Python, Matlab and Mathematica code used 48

B Sample properties and manual for reconstructing experiments 49
B.1 Manual for finding Intermodulation peaks using described setup . . . 50

C Symbolic regression 52
C.1 Coefficient scaling determination . . . 52
C.2 second iteration of coefficients determination . . . 56

D Determination of analytic relation between A_1 and A_3 61

Nomenclature

Abbreviations

Abbreviation	Definition
EoM	Equation of Motion
HB	Harmonic Balancing
LDV	Laser Doppler Vibrometer / Vibrometry
MSA	Micro System Analyser
DC	Direct current

Symbols

Symbol	Definition	Unit
γ	Non-linear cubic stiffness parameter	[m/s^2]
ω_0	Resonance Frequency	[Hz]
δ	Detuning	[Hz]
A_n	Amplitude at frequency n	[V_{pp}] or [m]

1

Introduction

The development of technology, and particularly the development of sensors and their ever-improving accuracy and precision, brings with it a shrinkage of said sensors. The development of nano-sensors resulted in a peculiar method to sense several different physical quantities by reading out the change in resonant frequency of a MEMS-sample. With this method, one can sense very small quantities of mass [22], pressure [10] [18], temperature [26], and more. However, the shift in resonant frequency is mostly non-linear in terms of the measured quantities.

Therefore, understanding the linear and non-linear dynamics of nanoscale resonators is particularly important. Mainly because of their many applications in the previously discussed areas of sensing, but also because of their applications in material characterisation, and nanoscale research. However, modelling their non-linear behaviour under excitation is computationally intensive and often impractical [1].

So there is a strong motivation to develop experimental methods for parameter estimation that do not rely solely on modelling. If the dynamics can be characterised directly from experiments, the governing parameters can be determined without requiring extensive numerical modelling of the system.

Most dynamical systems behave linearly when operating at small amplitudes, meaning that the response of an actuation at two frequencies is the response of the first frequency added to the response of the second frequency. When amplitudes become larger, non-linear effects emerge. In such systems, actuation with two frequencies results in sumfrequency terms next to the normal linear behaviour of the two applied tones. These sumfrequency terms can be used to characterise a dynamic system.

This two-tone characterisation of non-linearities is used in analysis of several types of non-linear dynamic systems like electrical systems [9] [25], radio frequency components [3] and in dynamics of MEMS [12], particularly on Duffing oscillators [8] [7] [23].

This thesis focuses on estimating non-linear parameters of dynamical systems with the use of two-tone excitation. By exciting a system with two tones, intermodulation products are generated at sum and difference frequencies, and their amplitudes can be used to estimate the non-linear parameter values. The work combines analytical, numerical, and experimental approaches to test whether intermodulation responses can be used to reliably estimate such non-linear parameters.

Thesis structure. Chapter 2 introduces the theoretical background, including non-linear oscillators and the harmonic balance method. Section 2.4 presents the derivation of analytic relations between intermodulation amplitudes. Chapter 3 Introduces the research question, research goals and methodology for achieving this. Chapter 4 describes the set-up that was used for the measurement of intermodulation products. Chapter 5 reports the numerical and experimental results, comparing analytic predictions with symbolic regression, direct integration, and measured data. Chapter 6 summarises the conclusions and provides recommendations for future work. and Chapter 7 discusses the implications of these findings.

2

Theory

For estimation of non-linear parameters, one needs to set a physical and mathematical basis of a dynamical model to describe the dynamics over time and/or frequency of a system. First it is looked into where non-linearities in dynamical systems, and clamped beams in general, come from in section 2.1. The mathematical description and derivation of the dynamical model are discussed in section 2.2. Then, in section 2.3, it is described how exciting this system with two tones can bring about intermodulation products that can be measured. Lastly, it is described how these intermodulation products can relate to the non-linear parameters in the mathematical model using harmonic balancing.

2.1. Origin of Non-linearities in Microsystems

Microsystems, such as the clamped nano-beams used in experiments in this study, exhibit strong non-linear behaviour even under extremely small excitation forces. These non-linearities arise primarily from geometric effects, which become significant at the nanoscale [2].

Some beams are intentionally pre-buckled to introduce bi-stability, allowing the system to occupy two stable equilibrium positions and rapid, stochastic switching between these when excited. This geometric change also introduces non-linear dynamical behaviour [11]. Altough these non-linearities are outside the scope of this thesis.

Additionally, the oscillation amplitudes in these systems are often large enough to induce parametric resonance. This occurs due to periodic variations in the length, stiffness, or other material properties of the clamped nano-beam when exciting the system. The mechanical properties of the system can in turn be non-linear in environmental conditions such as temperature, humidity or pressure [20].

Lastly, when multiple vibrational modes are active and the energy exchange between them becomes significant enough, the system may show mode coupling. This non-linear interaction between modes can lead to complex dynamics, including amplitude modulations, instabilities, or even chaotic motion. [14]

In this thesis, the cubic non-linear stiffness, or duffing oscillator, will be focussed on. For non-buckled samples, this non-linearity finds its origin in strain at large deflections. To derive this, a displacement function is made in the form of:

$$w(x,t) = \sum_{i=1}^{M} u_i(t)\phi_i(x) \text{ [24] [21]} \tag{2.1}$$

Where $w(x,t)$ is the displacement over time and location on the beam, M is the amount of considered modes, u_i is the generalized coordinate vector for mode i, $\phi_i(x)$ is the shape of the mode, usually modelled as $\phi_i(x) = sin(\frac{i\pi x}{L})$, where L is then length of the beam. For now, only one mode is considered

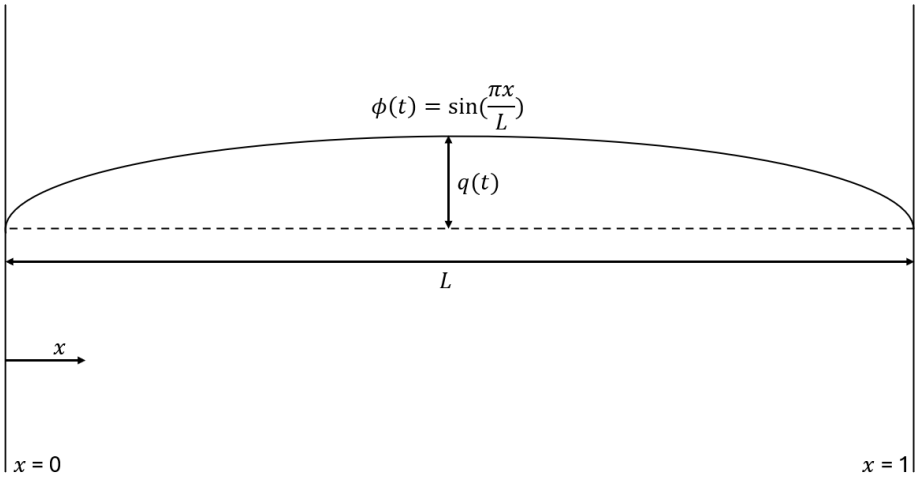

Figure 2.1: Representation of displacement function $w(x,t)$

so the displacement function will be as Equation 2.1 for $i = 1$. $u_1(t)$ will from now on be represented as $q(t)$. This $q(t)$ can also be interpreted as the displacement amplitude of the middle of the beam over time. A representation of this is given in Figure 2.1

When large excitation forces are applied on a double clamped beam, the displacement will be large enough so that the difference in beam length is significant enough for restoring forces to appear. The difference in length can be expressed by the difference in original length L and arc length S. A unit piece has length:

$$ds = \sqrt{dx^2 + dy^2} = \sqrt{1 + (\frac{dy}{dx})^2}\, dx$$

This can be rewritten by using the determined displacement function $w(x,t)$ from Equation 2.1 for a single mode.

$$\frac{dy}{dx} = \frac{\partial w(x,t)}{\partial x} = w'(x,t)$$

The arc length will then be the integral of all unit pieces over L:

$$S = \int_0^L \sqrt{1 + (w'(x,t))^2}\, dx$$

To simplify, a Taylor expansion is used to obtain:

$$\sqrt{1 + (w'(x,t))^2} = 1 + \frac{1}{2}(w'(x,t))^2 + \mathcal{O}\big((w')^4\big)$$

A new arc length can be set up in the form of:

$$S \approx \int_0^L (1 + \frac{1}{2}(w'(x,t))^2)dx = L + \frac{1}{2}\int_0^L (w'(x,t))^2 dx$$

And since the integral only depends on position, the time component can be gotten out of the integral.

$$\frac{1}{2}\int_0^L (w'(x,t))^2 dx = \frac{1}{2}\int_0^L (q(t)\cdot\frac{d\phi}{dx})^2 dx = \frac{1}{2}q^2(t)\int_0^L (\frac{d\phi}{dx})^2 dx$$

The difference in length between the curved position and neutral position can therefore be expressed as:

$$\Delta L = \frac{1}{2}q^2(t)\int_0^L (\frac{d\phi}{dx})^2 dx$$

Next, the strain energy can be calculated by using the axial force inside the beam in displaced position times the difference in length. This results in:

$$U_s = \frac{1}{2}EA\varepsilon\Delta L$$

$\varepsilon = \frac{\Delta L}{L}$

Where E is the Young's modulus of the material and A is the cross-sectional surface area of the beam. If the previously found relation is substituted in for ΔL, the strain energy will be:

$$U_s = \frac{EA}{2L}(\frac{1}{2}q^2(t)\cdot\int_0^L (\frac{d\phi}{dx})^2 dx)^2 = \frac{EA}{8L}q^4(t)\cdot(\int_0^L (\frac{d\phi}{dx})^2 dx)^2$$

For force equilibrium, the sum of the potential energy is differentiated over the generalised coordinate $q(t)$, which results in a cubic restoring force due to strain:

$$F_s = -\frac{\partial U_s}{\partial q} \propto q^3(t)$$

2.2. Mathematical modelling of a dynamic system

The dynamics of an oscillating system can be mathematically described by the vector equation 2.2. also known as the equation of motion (EoM). These kinds of linear equations are analytically solvable if the excitation force is not non-linear in time. Herein $\mathbf{M}$ is the mass matrix of the system, $\mathbf{C}$ the damping matrix and $\mathbf{K}$ the stiffness matrix. $\mathbf{F}$ is the excitation force vector.

$$\mathbf{M}\ddot{\mathbf{x}}(t) + \mathbf{C}\dot{\mathbf{x}}(t) + \mathbf{K}\mathbf{x}(t) = \mathbf{F}(t) \tag{2.2}$$

With non-linear equations of motion, it is difficult or even impossible to describe the displacement x(t) as a direct, analytic function of time. The solutions of non-linear equations are therefore mostly estimations. Non-linearities can have many sources, such as the geometry of the system, the internal mechanical properties of the materials of which the system is made, or outside influences such as electric or magnetic fields applying energy to the system. The non-linearities in the system are described by a function $\mathbf{\Gamma}(\mathbf{x}, \dot{\mathbf{x}}, t)$. This non-linearity function is for now only dependent on displacement, velocity, and time due to the non-linearities discussed in this thesis being of such nature that they depend on only these state variables. The resulting equation will become as shown in Equation 2.3.

$$\mathbf{M}\ddot{\mathbf{x}}(t) + \mathbf{C}\dot{\mathbf{x}}(t) + \mathbf{K}\mathbf{x}(t) + \mathbf{\Gamma}(\mathbf{x}, \dot{\mathbf{x}}, t) = \mathbf{F}(t) \tag{2.3}$$

In the samples that were available to measure, the Silicon-Nitride clamped beams, the non-linearities appear as a cubic stiffness.[2]. In the buckled variations of these samples, that will be discussed later, an extra non-linearity will be added that relates quadratically to displacement. In some systems there is an interaction between different modes so multimodal analysis needs to be performed [15] [5]. This

complicates the problem greatly and is outside the scope of this thesis. If only a single mode is to be analysed, the equation of motion will become as shown in Equation 2.4

$$m\ddot{x}(t) + c\dot{x}(t) + kx(t) + \beta x^2(t) + \gamma x^3(t) = F(t) \tag{2.4}$$

From this equation it is still difficult to measure mass, stiffness and damping terms to estimate what the relation between γ and β to these terms are. A mass normalised transformation (Equation 2.5) is therefore applied on Equation 2.3. Φ is the eigenvector matrix resulting from Equation 2.3. This transformation changes Equation 2.4 into Equation 2.6 [23], where ω_0 is the resonance frequency of the system and Q is the Q-factor of the system.

$$x(t) = \Phi q(t) \tag{2.5}$$

$$\ddot{q}(t) + \frac{\omega_0}{Q}\dot{q}(t) + \omega_0^2 q(t) + \tilde{\beta} q^2(t) + \tilde{\gamma} q^3(t) = \tilde{F}(t) \tag{2.6}$$

This resulting equation gives more insight and a simpler relation between the non-linear parameters and the measurable variables of the system. This $q(t)$ is the same modal coordinate vector as was explained in section 2.1.

2.3. Two tone excitation response of a dynamic system

When the model is excited with two tones, sumfrequencies will appear in the displacement solution of $q(t)$. This mixing of frequencies happens due to the quadratic and cubic stiffness terms. A two tone excitation example is given in Equation 2.7.

$$\tilde{F}(t) = f_1 cos(\omega_1 t) + f_2 cos(\omega_2 t) \tag{2.7}$$

To see why sumfrequencies appear, a simple two tone trial solution, or Ansatz, given in Equation 2.8, is substituted into Equation 2.6. What results is the appearance of sumfrequencies due to quadratic and cubic non-linearities as shown in Equation 2.9 and Equation 2.10. The sumfrequencies that appear are presented in Table 2.1

$$q_{trial}(t) = A_1 cos(\omega_1 t) + A_2 cos(\omega_2 t) \tag{2.8}$$

$$\begin{aligned} q_{trial}^2 &= A_1^2 cos^2(\omega_1 t) + A_2^2 cos^2(\omega_2 t) + A_1 A_2 cos(\omega_1 t) cos(\omega_2 t) \\ &= \frac{A_1}{2}(1 + cos(2\omega_1 t)) + \frac{A_2}{2}(1 + cos(2\omega_2 t)) + \frac{A_1 A_2}{2}(cos((\omega_1 + \omega_2)t) - cos((\omega_1 - \omega_2)t)) \end{aligned} \tag{2.9}$$

$$\begin{aligned} q_{trial}^3 = &\frac{A_1^3}{4}\left(3\cos(\omega_1 t) + \cos(3\omega_1 t)\right) + \frac{3A_1^2 A_2}{2}\left(1 + \cos(2\omega_1 t)\right)\cos(\omega_2 t) \\ &+ \frac{3A_1 A_2^2}{2}\cos(\omega_1 t)\left(1 + \cos(2\omega_2 t)\right) + \frac{A_2^3}{4}\left(3\cos(\omega_2 t) + \cos(3\omega_2 t)\right) = ... \end{aligned} \tag{2.10}$$

Type of non-linearity	Sumfrequencies
quadratic(β)	$2\omega_1, 2\omega_2, \omega_1 + \omega_2, \lvert\omega_1 - \omega_2\rvert$
cubic(γ)	$3\omega_1, 3\omega_2, 2\omega_1 \pm \omega_2, 2\omega_2 \pm \omega_1,$

Table 2.1: Sumfrequencies of the first order

When ω_1 and ω_2 are close together, the combination of certain sumfrequencies will result in a special phenomenon. This can be mathematically described as in Equation 2.11. Here δ is a detuning frequency. When this detuning is very low, the sumfrequencies at $2\omega_1 - \omega_2$ and $2\omega_2 - \omega_1$ will result in a response at a frequency that is 2δ away from the original exciation frequencies.

$$\begin{aligned} \omega_1 &= \omega - \delta \\ \omega_2 &= \omega + \delta \\ 2\omega_1 - \omega_2 &= 2(\omega - \delta) - (\omega + \delta) = \omega - 3\delta \\ 2\omega_2 - \omega_1 &= 2(\omega + \delta) - (\omega - \delta) = \omega + 3\delta \end{aligned} \tag{2.11}$$

When the frequencies that are given in Table 2.1 are also added to the the trial solution, higher orders of these sumfrequencies will appear, the most important of which according to Equation 2.12. If the same transformation is applied as in Equation 2.11 and ω is placed at resonance, then the sumfrequencies will eventually show up according to the relation given in Equation 2.13. This results in a frequency comb in the solution as seen in the example figure Figure 2.2.

$$\sum_{k=1}^{n} cos((k\omega_1 - (k-1)\omega_2)t) \quad \& \quad \sum_{k=1}^{n} cos((k\omega_2 - (k-1)\omega_1)t) \tag{2.12}$$

$$\sum_{k=0}^{n} cos((\omega \pm (2k+1)\delta)t) \tag{2.13}$$

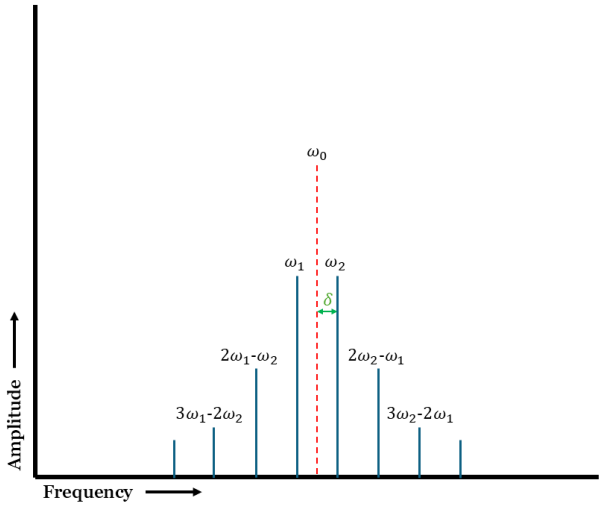

Figure 2.2: Intermodulation peaks example, frequency(Hz) vs. Amplitude(V)

2.4. Estimation of non-linear parameters using the Harmonic Balancing method

Subsequently, a relationship between the amplitude at the sum frequencies and the non-linear parameters can be investigated, as the peak amplitudes are experimentally measurable in the frequency

domain.

A generally applicable method to analytically find the approximate relation between frequency and amplitude is the method of harmonic balancing. With this method, an Ansatz is guessed and substituted into the EoM. Then, matching harmonics are grouped together and equalled to zero. In this way, an estimate relation between frequency and all other present parameters can be found analytically. A good initial guess is needed for Equation 2.6 to put out cosines of the right frequency.

First in subsection 2.4.1, it is looked into how the amplitudes can be related to the input parameters directly. This uses a trial solution consisting of cosines of the excitation frequencies, 3ω-harmonics, and first order sumfrequencies. Later in subsection 2.4.2 the indirect relation is investigated by looking at how the amplitudes at these frequencies relate to each other and how the system parameters come into play.

2.4.1. Sumfrequency amplitude estimation by Harmonic Balancing

As such, the basis of Harmonic balancing consists of taking the EoM and assuming an ansatz. Below there has been given an example on how relations can be found. This was done with Mathematica and the supplementary code can be found in Appendix A.

The first step is to take the EoM from which the non-linear parameters need to be estimated. This EoM is given in Equation 2.14. Compared to Equation 2.6, the damping and quadratic stiffness have been removed for simplicity and due to the samples that will be used to verify these results not exhibiting quadratic stiffness.

$$\ddot{q}(t) + \omega_0^2 q(t) + \gamma q^3(t) = f_1 cos(\omega_1 t) + f_2 cos(\omega_2 t)^* \tag{2.14}$$

*Where $\omega_1 = \omega_0 - \delta$ and $\omega_2 = \omega_0 + \delta$.

As a second step, an ansatz is chosen in which all the sum frequencies of order n are also included in the form of cosines. The ansatz for systems with only cubic stiffness of order 0 through 2 are as given in Equation 2.15. These ansatz's will be used in the analysis later on. The supplementary ansatz for systems with quadratic stiffness are as given in Equation 2.16. There is an extra DC component A_0 to accurately relate amplitude and frequency [19]. The amount of sumfrequencies that are chosen in the initial trial solution can be described as to which order Harmonic balancing is performed. This also amounts to k in Equation 2.12. For this example, only two orders are considered in the ansatz. For simplification reasons and in the light of previous observations, sumfrequencies that do not appear to have a large amplitude in reality, such as described in Table 2.1 are also not considered in the ansatz. These disregarded frequencies are not at a resonance frequency of samples that was used for measurements in this thesis. One needs to note that when there is noticable activity at one of these disregarded sumfrequencies, it needs to be considered in the ansatz for optimal accuracy.

$$\begin{aligned} q_0(t) &= A_1 cos(\omega_1 t) + A_2 cos(\omega_2 t) \\ q_1(t) &= q_0(t) + A_3 cos(3\omega_1 t) + A_4 cos(3\omega_2 t) + A_5 cos((2\omega_1 - \omega_2)t) + A_6 cos((2\omega_2 - \omega_1)t) \\ q_2(t) &= q_1(t) + A_7 cos((3\omega_1 - 2\omega_2)t) + A_8 cos((3\omega_2 - 2\omega_1)t) \end{aligned} \tag{2.15}$$

$$\begin{aligned} q_0(t) &= A_1 cos(\omega_1 t) + A_2 cos(\omega_2 t) \\ q_1(t) &= q_0(t) + A_0 + A_3 cos(2\omega_1 t) + A_4 cos(2\omega_2 t) + A_5 cos((\omega_1 + \omega_2)t) + A_6 cos((\omega_1 - \omega_2)t) \end{aligned} \tag{2.16}$$

For the case where only cubic non-linearity is considered, the ansatz of Equation 2.15, $q_1(t)$ is substituted for $q(t)$ in Equation 2.14. From the resulting equation the coefficients of the cosines of different frequencies that are also present in the ansatz are collected and equalled to zero. For the example of substituting Equation 2.15 in Equation 2.14, the resulting equations are listed below.

The equation for $cos(\omega_1 t)$:

$$\begin{aligned}
&-2F_1 + \frac{3}{2}A_1^3\gamma + 3A_1A_2^2\gamma + 3A_1A_2A_3\gamma + 3A_1A_3^2\gamma \\
&+ \frac{3}{2}A_2^2A_4\gamma + 3A_2A_3A_4\gamma + 3A_1A_4^2\gamma + \frac{3}{2}A_1^2A_5\gamma \\
&+ 3A_2A_3A_5\gamma + 3A_1A_5^2\gamma + 3A_2A_4A_6\gamma + 3A_1A_6^2\gamma \\
&+ 2A_1\omega_0^2 - 2A_1\omega_1^2 = 0
\end{aligned} \tag{2.17}$$

The equation for $cos(\omega_2 t)$:

$$\begin{aligned}
&-2F_2 + 3A_1^2A_2\gamma + \frac{3}{2}A_2^3\gamma + \frac{3}{2}A_1^2A_3\gamma + 3A_2A_3^2\gamma \\
&+ 3A_1A_2A_4\gamma + 3A_1A_3A_4\gamma + 3A_2A_4^2\gamma + 3A_1A_3A_5\gamma \\
&+ 3A_2A_5^2\gamma + \frac{3}{2}A_2^2A_6\gamma + 3A_1A_4A_6\gamma + 3A_2A_6^2\gamma \\
&+ 2A_2\omega_0^2 - 2A_2\omega_2^2 = 0
\end{aligned} \tag{2.18}$$

The equation for $cos(2\omega_1 - \omega_2)$:

$$\begin{aligned}
&\frac{3}{4}A_1^2A_2\gamma + \frac{3}{2}A_1^2A_3\gamma + \frac{3}{2}A_2^2A_3\gamma + \frac{3}{4}A_3^3\gamma \\
&+ \frac{3}{2}A_1A_2A_4\gamma + \frac{3}{2}A_3A_4^2\gamma + \frac{3}{2}A_1A_2A_5\gamma + \frac{3}{2}A_3A_4A_5\gamma \\
&+ \frac{3}{2}A_3A_5^2\gamma + \frac{3}{4}A_4^2A_6\gamma + \frac{3}{2}A_4A_5A_6\gamma + \frac{3}{2}A_3A_6^2\gamma \\
&+ A_3\omega_0^2 - 4A_3\omega_1^2 + 4A_3\omega_1\omega_2 - A_3\omega_2^2 = 0
\end{aligned} \tag{2.19}$$

The equation for $cos(2\omega_2 - \omega_1)$:

$$\begin{aligned}
&\frac{3}{4}A_1A_2^2\gamma + \frac{3}{2}A_1A_2A_3\gamma + \frac{3}{2}A_1^2A_4\gamma + \frac{3}{2}A_2^2A_4\gamma \\
&+ \frac{3}{2}A_3^2A_4\gamma + \frac{3}{4}A_4^3\gamma + \frac{3}{4}A_3^2A_5\gamma + \frac{3}{2}A_4A_5^2\gamma \\
&+ \frac{3}{2}A_1A_2A_6\gamma + \frac{3}{2}A_3A_4A_6\gamma + \frac{3}{2}A_3A_5A_6\gamma + \frac{3}{2}A_4A_6^2\gamma \\
&+ A_4\omega_0^2 - A_4\omega_1^2 + 4A_4\omega_1\omega_2 - 4A_4\omega_2^2 = 0
\end{aligned} \tag{2.20}$$

The equation for $cos(3\omega_1 t)$:

$$\begin{aligned}
&\frac{3}{4}A_2^2A_3\gamma + \frac{3}{2}A_1A_2A_4\gamma + \frac{3}{2}A_1A_3A_4\gamma + \frac{3}{4}A_2A_4^2\gamma \\
&+ \frac{3}{4}A_1^2A_6\gamma + \frac{3}{2}A_2A_3A_6\gamma + \frac{3}{2}A_1A_5A_6\gamma = 0
\end{aligned} \tag{2.21}$$

The equation for $cos(3\omega_2 t)$:

$$\begin{aligned}
&\frac{3}{2}A_1A_2A_3\gamma + \frac{3}{4}A_1A_3^2\gamma + \frac{3}{4}A_1^2A_4\gamma + \frac{3}{2}A_2A_3A_4\gamma \\
&+ \frac{3}{4}A_2^2A_5\gamma + \frac{3}{2}A_1A_4A_5\gamma + \frac{3}{2}A_2A_5A_6\gamma = 0
\end{aligned} \tag{2.22}$$

These equations become quite convoluted when attempting to solve analytically and result in solutions with multiple roots. One can imagine the complexity of the equations at higher order analysis. The trick that is therefore applied is to group the coefficients in order of magnitude [19]. Amplitudes of first-order ansatz, $A_1 \& A_2$ are assigned order $\mathcal{O}(1)$, second-order amplitudes, A_3, A_4, A_5, A_6 are given order $\mathcal{O}(3)$. $A_7 \& A_8$ will be given order $\mathcal{O}(5)$. This way, the reduced equations become simpler and the results can be described analytically instead of roots of convoluted third-order polynomials. If the equations are taken with coefficients up to order $\mathcal{O}(3)$, then the equations result in relations as seen in Equation 2.23. These findings match those found in the thesis of Wattjes [23].

$$\begin{aligned}
A_5 &= -\frac{3A_1^2A_2\gamma}{4\left(\omega_0^2 - 4\omega_1^2 + 4\omega_1\omega_2 - \omega_2^2\right)} \\
A_6 &= -\frac{3A_1A_2^2\gamma}{4\left(\omega_0^2 - \omega_1^2 + 4\omega_1\omega_2 - 4\omega_2^2\right)}
\end{aligned} \tag{2.23}$$

For more accuracy, higher order analysis is needed. Higher order analysis results in convoluted equations with rooted analytical solutions. There are methods to essentially take a shortcut in solving these relations like symbolic regression and Taylor expansions. It is therefore later looked into how the different amplitudes at sumfrequencies can numerically relate to each other to find a relation between individual amplitudes and input parameters.

2.4.2. Analytically Relating Sumfrequency Amplitudes to Excitation Amplitudes and system parameters

To get a better understanding of how the parameters relate, a study can be done on the relation between the amplitudes with each other. For an analysis with as little parameters as possible, some definitions are adjusted. The Amplitudes A_1 through A_8 are redefined as described in Figure 2.3 below.

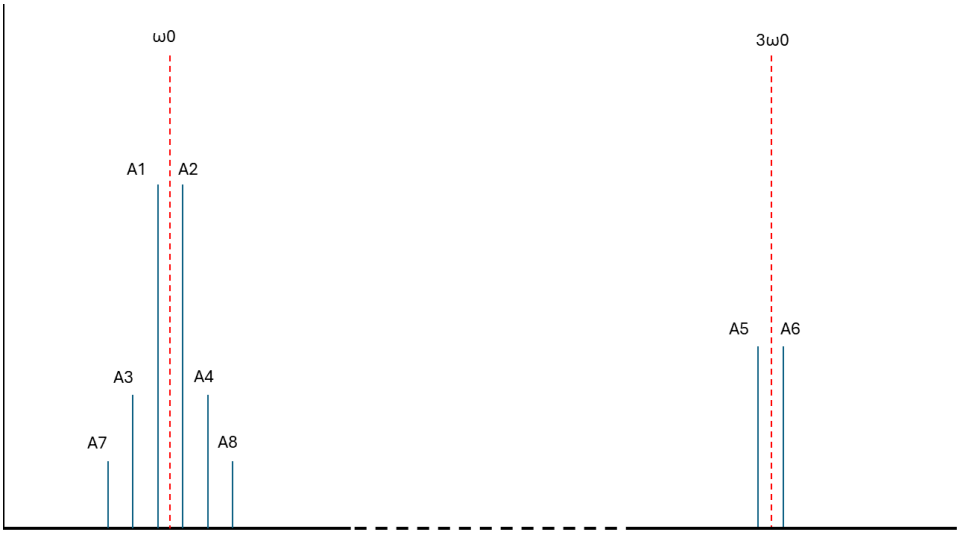

Figure 2.3: Definition of amplitudes

The relation between A_5 and A_6 to the system parameters is easy to analytically acquire from harmonic balancing, more specifically the solution of Equation 2.21 and Equation 2.22 of order $\mathcal{O}(3)$. These relations are cubic in A_1 and A_2 respectively. A_5 and A_6 are described in Equation 2.24.

$$\begin{aligned} A_5 &= -\frac{A_1^3\gamma}{4(\omega_0^2 - 9\omega_1^2)} \\ A_6 &= -\frac{A_2^3\gamma}{4(\omega_0^2 - 9\omega_2^2)} \end{aligned} \tag{2.24}$$

These relations can be substituted for A_5 and A_6 in the previously described equations that result from harmonic balancing. After this substitution, six equations with six unknowns remain. This means that the system is solvable.

To relate the remaining amplitudes to each other, there are two paths to a solution. The first is a direct analytic solution of the equations. The second is the application of a numerical solver to the equations Equation 2.17 to Equation 2.22. This numerical symbolic regression is further executed in subsection 5.1.2. In this section, the analytic relations between A_1 through A_8 will be studied.

When trying to analytically solve six equations with 6 unknowns and 3 more independent parameters, assumptions and choices need to be made. Therefore, relations between certain amplitudes will need to be studied. Since A_7 and A_8 were observed to be non-observable or small in most experimental results, these were not considered for the analytic relation. A_1 and A_2 are good candidates for relation because they are always present in a dynamic system due to these amplitudes being at the excitation frequencies. The disadvantage, however, is that the relation between A_1 and A_2 greatly corresponds to the linear system parameters and does not tell anything about the non-linear behaviour of the system. The relation between A_1 and A_2 can be obtained from solving Equation 2.17 for A2 for coefficients up to order 3. The result can be seen in Equation 2.25. The order of A_1 in this equation can be analysed and rewritten into a close to linear relation. That means that according to this theory, the two excitation

tones will behave according to a combination of a linear function in A_1 and a function that is proportional to $A_1^{-\frac{1}{2}}$.

$$A_2 \;=\; -\sqrt{\frac{4F_1}{6\gamma A_1} - \frac{1}{2}A_1^2 + \frac{2}{3}\frac{\delta}{\gamma}(\delta - 2\omega_0)} \tag{2.25}$$

When Taylor expansion is performed, this transforms into Equation 2.26

$$\begin{aligned} A_2 =& \frac{1}{128\sqrt{6}F_1^5\sqrt{\frac{A_1\gamma}{F_1}}} \cdot \Big(-256F_1^5 + 32F_1^4(3A_1^3\gamma - 4A_1\delta(\delta - 2\omega_0)) \\ & - 16A_1^2F_1^3\delta(3A_1^2\gamma - 2\delta(\delta - 2\omega_0)) \cdot (\delta - 2\omega_0) \\ & + 4A_1^3F_1^2\delta^2(9A_1^2\gamma - 4\delta(\delta - 2\omega_0)) \cdot (\delta - 2\omega_0)^2 \\ & + 10A_1^4F_1\delta^4(\delta - 2\omega_0)^4 - 7A_1^5\delta^5(\delta - 2\omega_0)^5\Big) \end{aligned} \tag{2.26}$$

A_3 and A_4 are therefore optimal candidates and even better when also relating them to the excitation amplitudes A_1 and A_2. Then there is a connection between excitation and non-linear effects that can be exploited to estimate non-linear cubic stiffness γ. The relation between A_1 and A_3 was chosen for analysis. When Harmonic Balancing is performed and certain assumptions are done, the relation of A_1 and A_3 will be in the form of Equation 2.27. A derivation of this relation and the assumptions that are made is explained in more detail in Appendix D.

$$A_3 = -\frac{-A_1^5\gamma^2 - 18A_1^3\gamma\delta^2 + 36A_1^3\gamma\delta\omega_0 - 16A_1^3\gamma\omega_0^2}{8\big(A_1^2\gamma - 3\delta^2 + 2\delta\omega_0\big)\big(9\delta^2 - 18\delta\omega_0 + 8\omega_0^2\big)} \tag{2.27}$$

This is a concrete relation that can be tested against numerical simulation data as well as experimental data.

This function is analysed on the effects of the individual parameters. Generally, this function represents a polynomial of fifth order for lower values of A_1 and a third order polynomial for high values of A_1 due to the presence of A_1^5 in the numerator and the presence of A_1^2 in the denominator. This is further proven by taking the Taylor series approximation of the function, presented in Equation 2.28.

$$A_3 \;=\; \frac{\gamma A_1^3}{4\delta\,(3\delta - 2\omega_0)} + \frac{\big(7\gamma^2\delta - 8\gamma^2\omega_0\big)\,A_1^5}{8\delta^2\,(3\delta - 4\omega_0)\,(3\delta - 2\omega_0)^2} + \mathcal{O}\big(A_1^7\big)\,. \tag{2.28}$$

As an example, the effects of δ, γ and $\omega_0 0$ are presented in the figures 2.4 to 2.6 below.

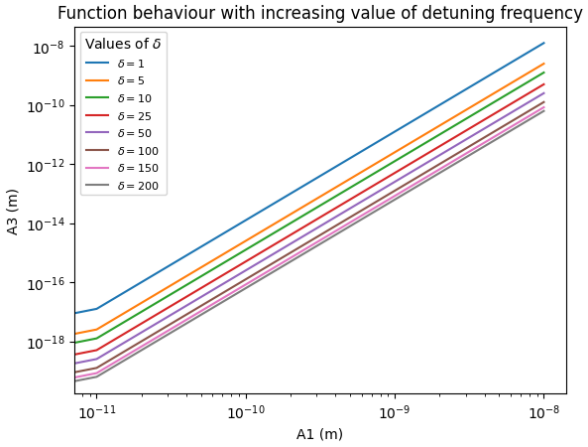

Figure 2.4: The effect of an increase in detuning frequency δ on the analytic relation

It makes sense that with a higher detuning frequency, the amplitude of the sumfrequency component becomes smaller because the two excitation frequencies are further apart and do not lie in the non-linear regime of the resonance any more for a sufficiently high δ.

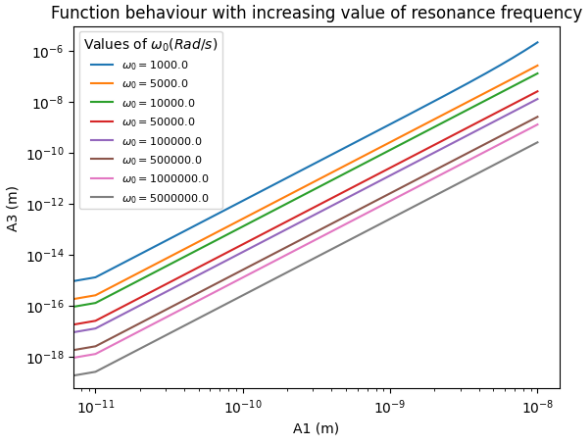

Figure 2.5: The effect of an increase in resonance frequency ω_0 on the analytic relation

When the resonance frequency increases, the amplitude of the sumfrequency component drops. This is likely due to the stiffness directly being proportional to the resonance frequency squared. If the excitation force remains at an equal level, it generates a lower displacement, thus amplitude, on systems with higher stiffness.

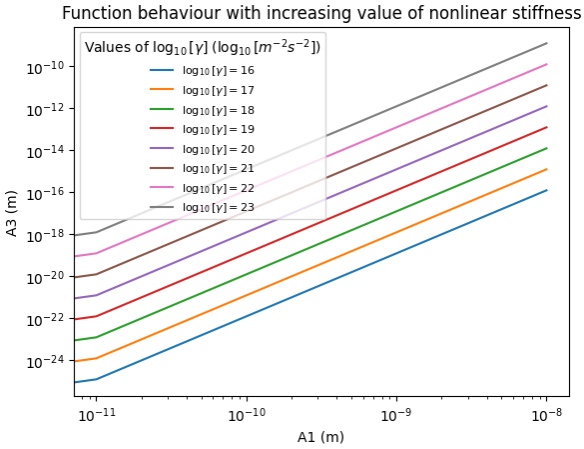

Figure 2.6: The effect of an increase in non-linear stiffness γ on the analytic relation

It can be seen that when the non-linear stiffness is increased, the magnitude of the first-order sum-frequency amplitude becomes higher and even surpasses the amplitude of the excitation frequency component. This makes sense due to the non-linearity being the source of these sumfrequencies.

All in all, the function seems to display similar behaviour to what is expected.

This cubic nature of the analytic relation from Equation 2.28 can be attempted to be validated by deriving it directly from the resulting amplitude when an ansatz of $q(t) = A_1 cos(\omega_1 t) + A_2 cos(\omega_2 t)$ is inserted into Equation 2.14. This results in the previously discussed Equation 2.10. The $\gamma q^3(t)$ term will generate a sumfrequency component at $2\omega_1 - \omega_2$ with amplitude $\frac{3}{4} A_1 A_2^2 \gamma$ which is a function of the third power of the excitation amplitudes. This corresponds to the cubic nature in the analytic relation of Equation 2.28.

3

Methodology

The aim of this thesis is to investigate whether the analytic relations, developed in Chapter 2 accurately describe the non-linear behaviour of certain dynamic systems under two-tone excitation. To achieve this, a combination of numerical simulations and experimental measurements is employed. The methodology is structured around three main steps: (i) numerical simulations based on the numeric solving of the equations that resulted from performing harmonic balancing, (ii) numeric integration of the non-linear equation of motion, and (iii) validation through experimental data and estimation of non-linear cubic stiffness.

First, the set of non-linear algebraic equations obtained from harmonic balancing (see Section 2.4) is numerically solved in Mathematica. This approach allows comparison these numerical results to the derived analytical relationship between the cubic stiffness parameter γ, the resonance frequency ω_0, the detuning frequency δ, and the amplitudes of the intermodulation products. These results are then also used to derive complementary approximate relations using symbolic regression. This may improve the analytic relation between amplitudes by eliminating the need for assumptions. Second, the non-linear equation of motion (Equation 2.14) is solved directly in the time domain using a numerical solver implemented in Python. In this approach, the system is excited with varying driving forces, and the resulting steady-state responses are analysed to extract the amplitudes at both excitation and intermodulation frequencies. By comparing the outcomes of the direct solver with those of the harmonic balancing approach, the consistency of the theoretical predictions can be assessed.

Finally, the analytical relation is validated against experimental measurements performed on Silicon-Nitride clamped nano-beams. The experimental data provide frequency response curves and intermodulation spectra over varying excitation forces that can be directly compared to the theoretical and numerical predictions. This validation step ensures that the analytic relation derived from the harmonic balancing method is not only mathematically consistent but also physically meaningful in describing real systems.

3.1. Research Question

The central research question of this thesis is:

> **How can intermodulation responses under two-tone excitation be used to estimate the non-linear stiffness parameters of dynamic systems?**

3.1.1. Sub-questions

To address this main question, the following sub-questions are formulated:

1. How can harmonic balancing be applied to derive analytical relations between intermodulation amplitudes and non-linear stiffness parameters?
2. To what extent do direct numerical simulations of the non-linear equation of motion confirm these analytical harmonic balancing relations?

3. How well do the theoretical and numerical results correspond to experimentally measured intermodulation peak relations?

3.1.2. Research Goals

The specific goals of this thesis are:

- To derive and solve relations between intermodulation amplitudes and non-linear parameters using harmonic balancing.
- To implement and validate a direct numerical solver for the non-linear equation of motion.
- To experimentally measure intermodulation peaks and compare them with theoretical and numerical predictions.
- To evaluate the sensitivity of non-linear parameter estimation to sample geometry and experimental conditions.

4

Experimental Set-up

This chapter describes the setup that was used to find intermodulation peaks with high resolution and in a robust, repeatable manner. Robust meaning: every experiment outputs the same results, also when done at a different time or temperature. And repeatable meaning: the experiments can be done multiple times and will not fail to work when done with other settings in the code. The system was set up in such a way that the input and the output would be the same in every repetition of the measurements with the same parameters. A detailed description and manual on how to find the intermodulation peaks is provided in Appendix B.1. The goal of the setup is to extract frequency data of a clamped nano-beam sample that is excited by two signals with slightly different frequencies. The setup must do this by exciting a piezo-actuator on which a chip is located with clamped nano-beam samples with varying thickness, clamp length and clamping buckling angle. The setup used a Polytec laser doppler vibrometer (LDV) of type MSA-500 to obtain velocity data of the sample over time. The higher the velocity, the higher the voltage of the output.

4.1. Overview of the Setup

The setup that was used required high accuracy in generating signals and extracting signals with frequencies between 100 kHz and 1 MHz. First, a computer is needed to compute and convert the electrical signals to usable data and control the input signal. This input signal is fed into a Moku:Lab to make this device generate two cosine waveforms at different frequencies. The same Moku:Lab is also used as a spectrum analyser for converting output signals to the frequency domain. The Moku:Lab was chosen due to the supervisors previous experience with this exact device, the high user-friendliness of the device and a great documentation of the Python and Matlab API to write algorithms to make the device do what is required. The Piezo-electric actuator could only handle a single input so the two input signals that were generated by the Moku:Lab device were combined into a single signal. While the piezo-electric actuator could handle a 10 Volt input, the Moku:Lab could only generate signals up to 2 Vpp. It was also discovered that the power combiner was non-linear when inputting two signals above 0.8 Vpp. A detailed analysis of the non-linearities of the power combiner can be found in subsection 4.2.1.

Due to the maximum output voltage of the power combiner only being 1 Vpp and the usual excitation voltage of the piezo-electric actuator being 10 Vpp, the results that were achieved with this current setup did not show any sign of non-linearities in the clamped beam. This is further illustrated by Figure 4.1.

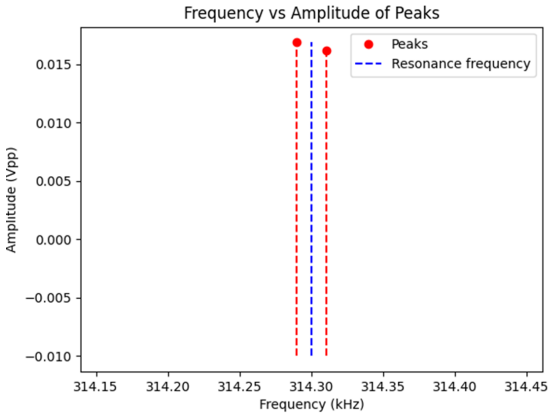

Figure 4.1: No present non-linearities close to the excitation frequencies

It was thus only excited into linear behaviour at that time. To counteract this and excite the clamped beam into its non-linear regime, a power amplifier was added. It amplified the incoming signal by a factor 20. Later it was discovered that acquired results would seemingly mean that the system was excited into its non-linear regime, even with low excitation force so the amplifier was investigated and it was found that at frequencies above 480 kHz the amplifier would also seem to apply a cubic non-linearity to the input signal and cause amplitudes at sumfrequencies. This is seen in Figure 4.2 and Figure 4.3.

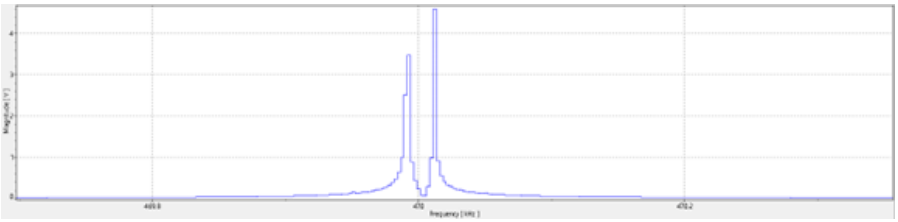

Figure 4.2: Wanted input signal, two pure tones

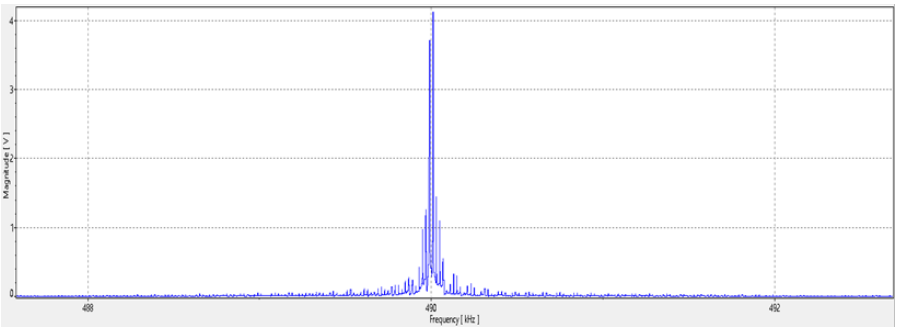

Figure 4.3: Unwanted input signal, added non-linearity

Therefore, two decisions were made. One was that the input signal into the piezo-electric actuator should be monitored by an external spectrum analyser at all times to make sure that the input signal is a linear combination of the two excitation signals. Another decision was made to only analyse the clamped beam samples that have a resonance frequency below 450 kHz since this is sufficiently below the threshold of 480 kHz to make sure there are no unwanted sumfrequencies in the input signal. An overview of the resonance frequencies of the samples can be found in B.

After the input signals were generated by the Moku:Lab, combined by the power combiner and amplified by the amplifier, the signal was split with a splitter and fed into the piezo-electric actuator and the previously mentioned external spectrum analyser. The Polytec LDV MSA-500 was used to extract the velocity of the sample over time. This signal is fed into the Moku:Lab for spectrum analysis. This all was controlled by a computer with Python and Matlab scripts that are also supplied in Appendix A.

An overview of the setup can be seen in Figure 4.4 in the form of a flowchart.

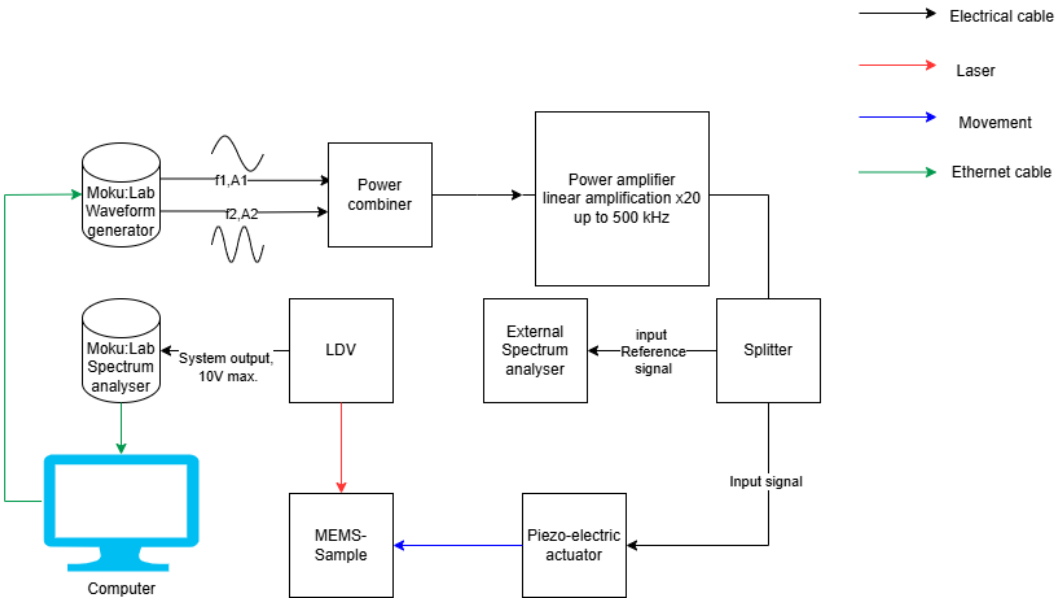

Figure 4.4: Used setup for measurements

4.2. Non-linearities in the input signals due to components set-up

During the time of this study it was found that some used components exhibited non-linear behaviour in certain circumstances. This affects the accuracy and validity of the results by introducing unwanted side effects. To counteract these non-linearities it was investigated under which circumstances these non-linearities occurred.

4.2.1. Non-linearity in the Input Signal due to the Power Combiner

The power combiner was seen to behave non-linearly in certain configurations. The effect of the change of setting parameters is shown in the following figures. The input signals were kept at equal voltages. The power combiner was tested for -20dB attenuation in the Moku:Lab and for 0dB attenuation, of which the results can be seen in Figure 4.5 and Figure 4.6 below.

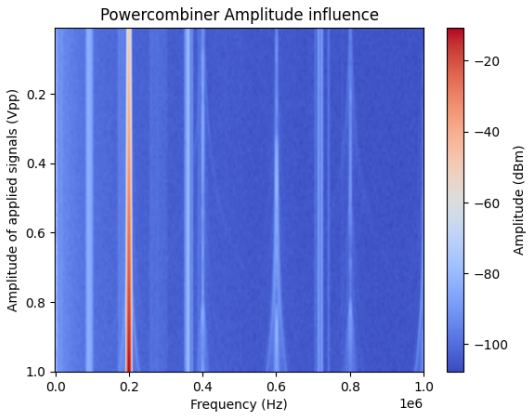

(a) Power combiner output at 0dB attenuation

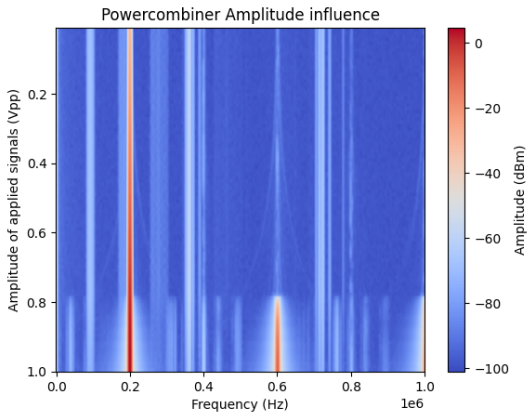

(b) Figure 2

Figure 4.5: Amplitude influence of powercombiner output

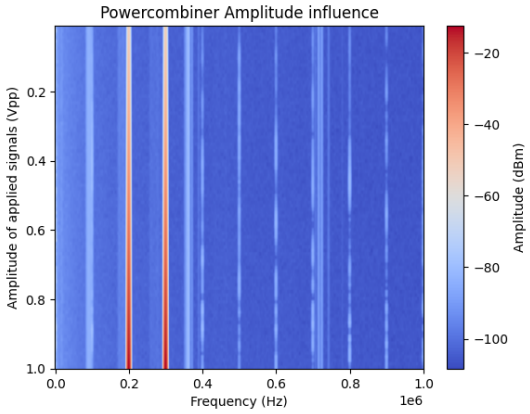

(a) Power combiner output at 0dB attenuation

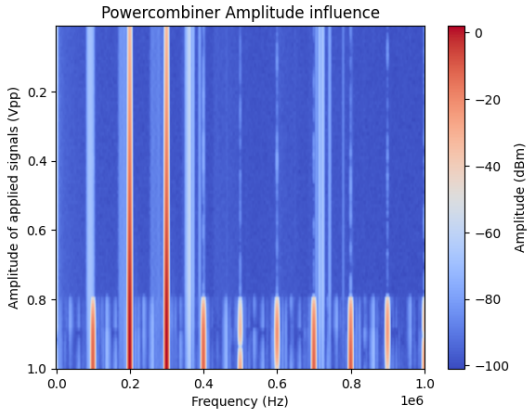

(b) Figure 2

Figure 4.6: Amplitude influence of power combiner output with high detuning δ

What can be seen is that there are non-linear artifacts of the power combiner or Moku:Lab itself after a combined amplitude of 0.8 Vpp. This was later assumed to be originating from the Moku:Lab itself because at this point, the Moku:Lab outputs signals of an amplitude close to its maximum output voltage of 2 Vpp [13].

Another parameter that can be varied and have influence on the power combiner is the detuning, this indicates how far away the two tones are placed in terms of frequency. This was investigated at an amplitude above 0.8 Vpp and below. The results are shown in Figure 4.7aFigure 4.7b what can be seen is that in the analysis above 0.8 Vpp amplitude, frequencies appear in the output of the power combiner at 3x the input frequencies, this indicates a cubic non-linearity. It must be noted that the y-axis is wrongly given a linear magnitude while it should be logarithmic from 0 to 1e6 Hz difference between the two signals

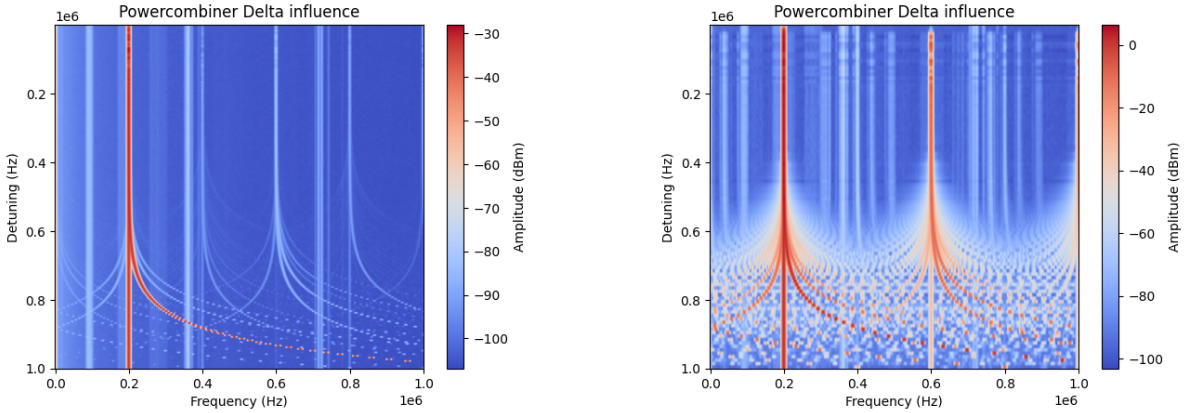

(a) analysis at low amplitude

(b) analysis at high amplitude

Figure 4.7: Detuning influence of power combiner output with varying detuning δ

5

Results

In this chapter, the outcomes of the comparison between analytical and numerical analyses are presented. The aim is to clarify how different intermodulation peaks are theoretically related to one another and how they depend on the cubic non-linear stiffness parameter γ. Two complementary numerical approaches were employed. The first approach involved solving the set of equations (Equations 2.17–2.22) obtained through the harmonic balancing method. From these solutions, approximate functional relations can be derived that link γ to the other relevant system parameters and the amplitude of intermodulation products. The second approach consisted of directly simulating the system dynamics using the transformed equation of motion (Equation 2.14), which was solved numerically with the RK-45 numerical integration method in Python. By comparing the results of these two independent methods with the analytical relation in the form of Equation 2.27, the consistency and limits of the analytic relation can be assessed. Finally, the analytical solution is compared with experimental measurements to evaluate whether it can accurately describe the dynamics of the system. In cases where similarity is observed, the non-linear stiffness parameter is estimated from the experimental data.

5.1. Comparing the Analytic Solution to Numerical Solutions

In this section, the analytic relationship in Equation 2.27, which relates A_1 to A_3, is tested for accuracy by numerically solving the harmonic balancing equations under varying excitation forces (subsection 5.1.1). In subsection 5.1.3, the analytic relation is further compared to direct numerical integration results. For both comparisons, the validity of the analytic approximation is quantified by computing R^2-values between the analytic expression and the numerical data, thereby indicating the parameter ranges in which the analytic solution can be applied with confidence.

For clarity, the analytic relation of Equation 2.27 is repeated below as Equation 5.1.

$$A_3 = -\frac{-A_1^5\gamma^2 - 18A_1^3\gamma\delta^2 + 36A_1^3\gamma\delta\omega_0 - 16A_1^3\gamma\omega_0^2}{8\big(A_1^2\gamma - 3\delta^2 + 2\delta\omega_0\big)\big(9\delta^2 - 18\delta\omega_0 + 8\omega_0^2\big)} \tag{5.1}$$

5.1.1. Comparing the Analytic Solution to Numerical Solutions of the HB-equations

The first numerical analysis is based on the harmonic balancing relations derived in section 2.4. The set of non-linear harmonic balancing equations (Equation 2.17 to Equation 2.22) was solved numerically for varying values of the cubic stiffness parameter γ, the resonance frequency ω_0, and the detuning parameter δ. For simplicity, the two excitation forces were taken equal, i.e. $F_2 = F_1 = f$. This force f was swept over a range that results in response amplitudes comparable to those of dynamical systems with nanometre- to millimetre-scale displacements.

To improve convergence, a continuation approach was adopted: for each step in excitation force, the previous solution for amplitudes A_1 to A_8 was used as the initial guess. The solutions were then plotted and compared with the analytic relation of Equation 5.1 for the same input parameters. Representative examples are shown in Figure 5.1.

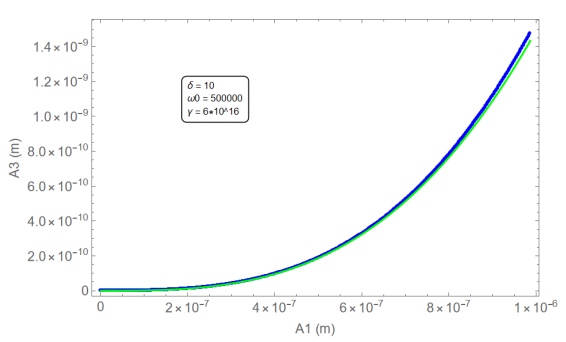

(a) $\gamma = 6 \cdot 10^{16}$ m^{-2}s^{-2}, $\omega_0 = 5 \cdot 10^5$ Rad/s, $\delta = 10$ Rad/s.

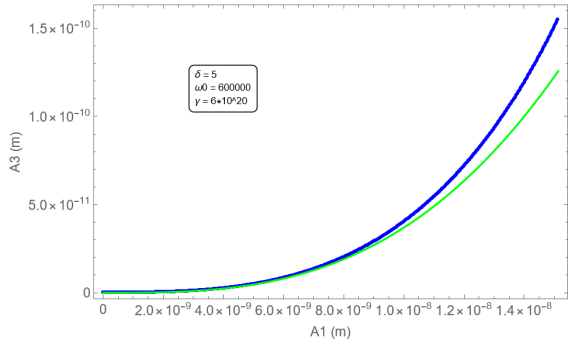

(b) $\gamma = 6 \cdot 10^{20}$ m^{-2}s^{-2}, $\omega_0 = 6 \cdot 10^5$ Rad/s, $\delta = 5$ Rad/s.

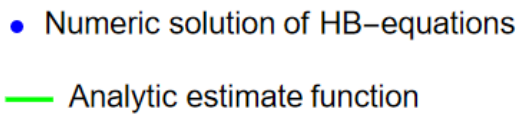

(c) Legend

Figure 5.1: Comparison of numeric solutions of the HB-equations with the analytic relation for two parameter sets.

For some parameter sets, the analytic relation reproduces the A_1–A_3 curve closely, whereas in other cases it diverges. To systematically map the regions of validity, the maximum amplitude for which the analytic and numerical relations maintain an error of $|R^2 - 1| \leq 0.1$ was determined. This maximum amplitude is shown in Figure 5.2 for varying combinations of γ, ω_0, and δ. Black pixels indicate parameter ranges where no agreement is found, suggesting that the analytic relation is not applicable.

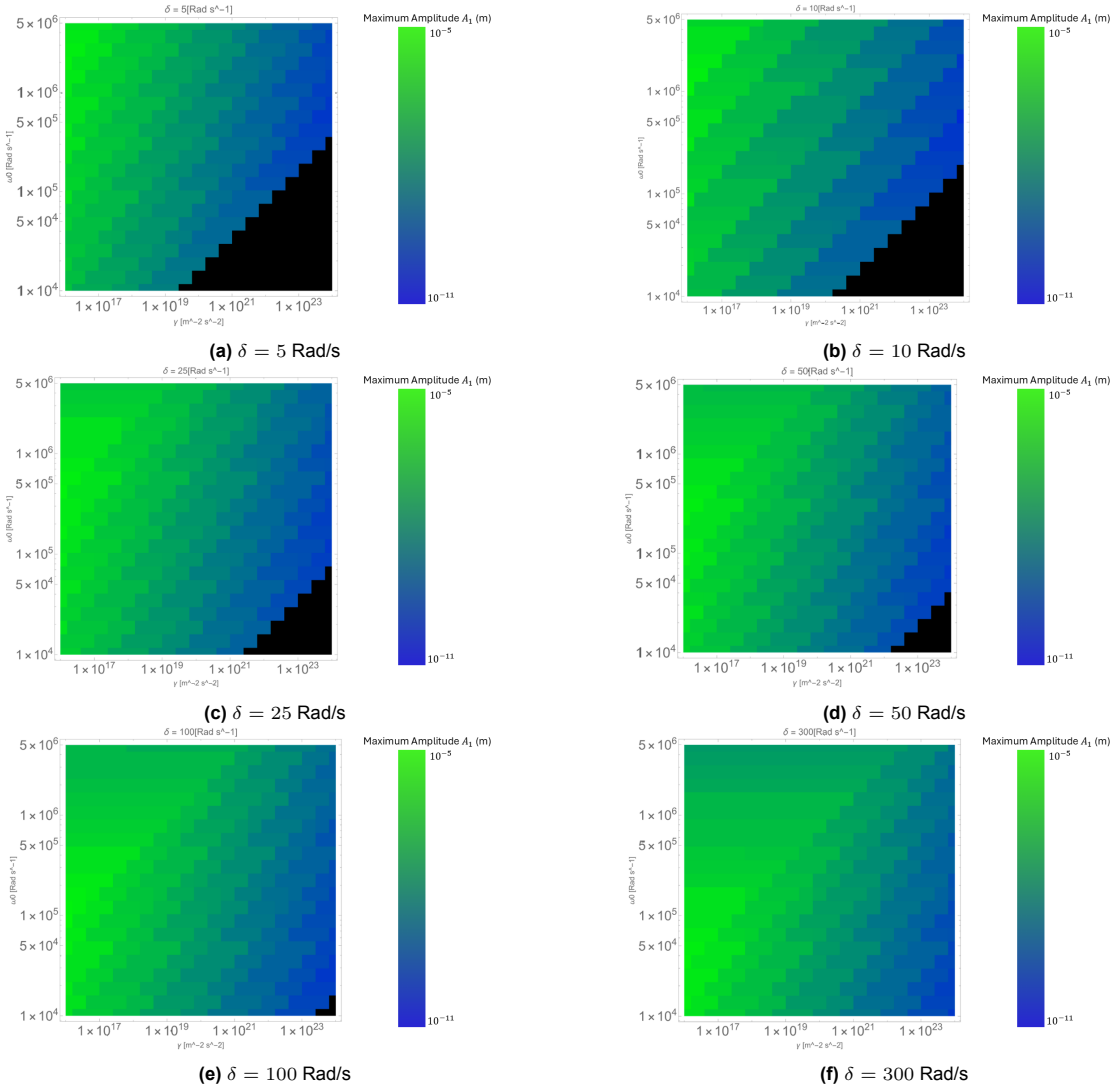

(a) $\delta = 5$ Rad/s **(b)** $\delta = 10$ Rad/s

(c) $\delta = 25$ Rad/s **(d)** $\delta = 50$ Rad/s

(e) $\delta = 100$ Rad/s **(f)** $\delta = 300$ Rad/s

Figure 5.2: Maximum amplitude for which the R^2-error between the analytic relation and the numerical solution is less than 0.01 for various parameter sets.

Two main factors explain why the analytic relation fails in certain regions. First, the HB-equations are six coupled third-order polynomials, which allow multiple solution branches. Such branching (see Figure 5.3) causes deviations from the simplified analytic curve. Second, the analytic derivation relies on assumptions, such as neglecting the amplitudes A_7 and A_8. At higher excitation forces or when γ/ω_0 increases, second-order intermodulation products become significant, influencing the first-order peaks and thereby reducing the accuracy of the simplified expression.

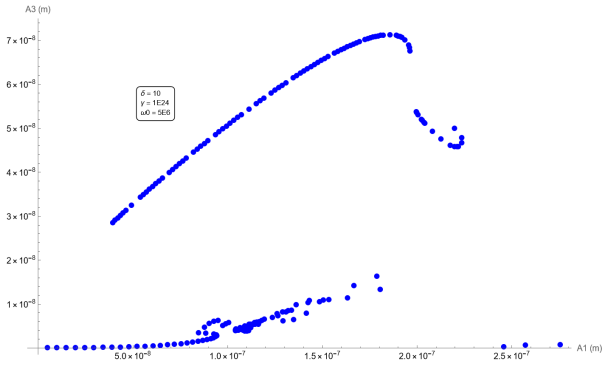

Figure 5.3: Example of solution branching in the HB-equations.

Interestingly, increasing the detuning frequency enlarges the parameter space in which the analytic relation remains valid. In particular, for high γ and low ω_0, higher detuning allows accurate estimation at low amplitude levels. Presumably this effect is caused by the fact that non-linearities appear sooner when the difference in frequency between excitation tones is smaller. This difference in excitation tones is captured by this detuning parameter δ.

5.1.2. Symbolic Regression of Numerical Solutions of HB-equations as Aid and Comparison

In addition to the analytic relation, it was investigated whether symbolic regression could simplify the estimation of non-linear cubic stiffness. In this section, the results of this approach are presented. Symbolic regression was carried out by explicitly solving the harmonic balancing equations and subsequently fitting algebraic expressions to the obtained data. First, to compare the outcome of this approach with the previously derived analytic relation, and second, to assess whether symbolic regression could provide accurate relations in parameter regions where the analytic expression fails to capture the amplitude–amplitude behaviour.

A key advantage of this method is that it avoids direct time-domain integration of the non-linear equation of motion, instead relying on algebraic relations between amplitudes at sumfrequencies obtained through harmonic balancing. Moreover, unlike the analytic derivation, symbolic regression does not require limiting assumptions, and may therefore come to a more accurate approximations in cases where such assumptions break down. Numerical solutions were obtained using *Wolfram Mathematica*, chosen for its better symbolic and numerical solving capabilities compared to Python or MATLAB, which are less efficient in handling the algebraic complexity of harmonic balancing equations.

The same harmonic balancing relations derived in section 2.4 (Equation 2.17–Equation 2.22) were solved numerically for varying values of γ, ω_0, and δ. For simplicity, the excitation forces were taken equal, i.e. $F_2 = F_1 = f$. This differs from the analytic derivation, where the amplitudes A_1 and A_2 were assumed equal. The force f was swept over a range such that the resulting amplitudes correspond to realistic dynamical systems. The focus was on amplitude ranges between 10^{-11} m and 10^{-7} m, relevant for systems such as graphene drums, which are known to be highly non-linear. In these systems, cubic stiffness values range between $10^{16}\,\mathrm{N}/(\mathrm{kg\,m^3})$ and $10^{25}\,\mathrm{N}/(\mathrm{kg\,m^3})$, with resonance frequencies between $5 \cdot 10^4$ Hz and $5 \cdot 10^6$ Hz.

The first step was to determine the general form of the A_1–A_3 relation for different parameter sets. Figures 5.4 to 5.6 illustrate typical results. Because of the cubic non-linearity, one might expect A_3 to follow a cubic dependence on A_1. However, as shown in Figure 5.4, the observed relation deviates significantly from a purely cubic form. In Figure 5.5, adding a quadratic term improves the fit but does not fully capture the behaviour. In Figure 5.6, a quintic polynomial provides an excellent fit, with $R^2 = 1$. The assumed form of the relation is therefore a fifth-order polynomial in A_1, given in Equation 5.2. No constant term is included, since at zero excitation both linear and non-linear effects vanish.

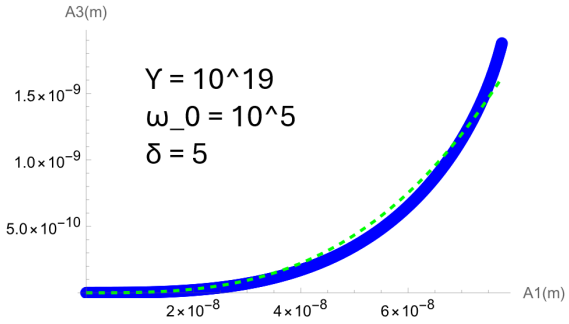

Figure 5.4: A_1–A_3 relation for parameter set 1.

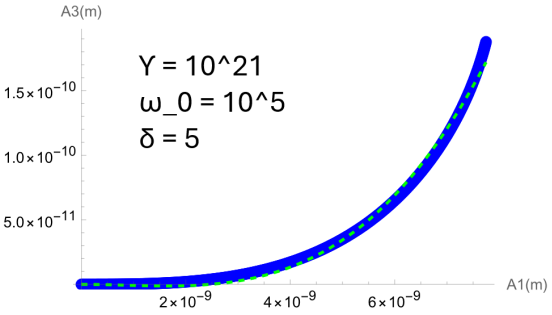

Figure 5.5: A_1–A_3 relation for parameter set 2.

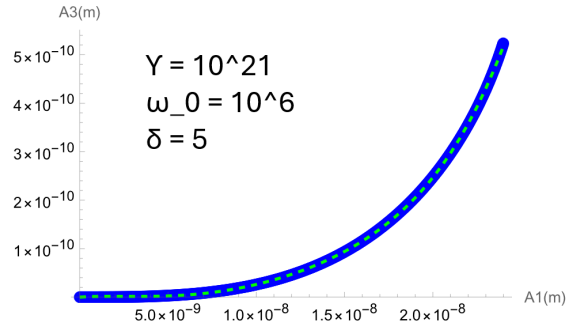

Figure 5.6: A_1–A_3 relation for parameter set 3.

$$A_3 = aA_1^5 + bA_1^4 + cA_1^3 + dA_1^2 + eA_1 \tag{5.2}$$

Next, the dependence of the coefficients a, b, c, d, and e on γ, ω_0, and δ was investigated. Figures 5.7 to 5.9 show, as an example, how coefficient a varies with γ for different values of ω_0. A fit was performed in each case to determine scaling laws. On the x-axis, the relevant range of γ corresponding to amplitudes between 10^{-10} m and 10^{-7} m is indicated.

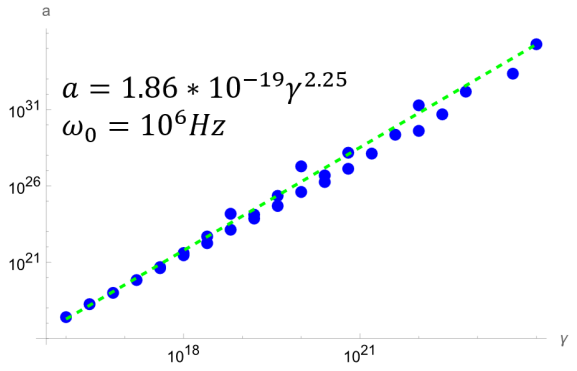

Figure 5.7: Coefficient a as a function of γ for $\omega_0 = 10^6$ Hz.

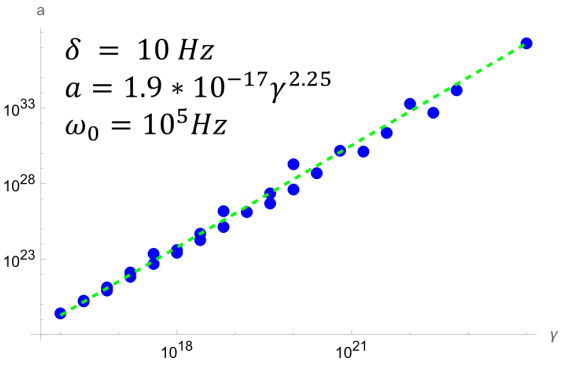

Figure 5.8: Coefficient a as a function of γ for $\omega_0 = 10^5$ Hz.

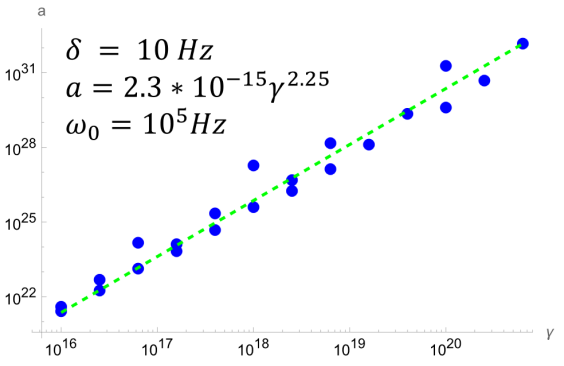

Figure 5.9: Coefficient a as a function of γ for $\omega_0 = 10^4$ Hz.

A similar analysis was performed for b, c, d, and e. The full set of results is provided in Appendix C. The overall dependencies are:

$$\begin{aligned} a &\propto \gamma^{2.25}, \\ b &\propto \gamma^{2}, \\ c &\propto \gamma^{1}, \\ d &\propto \gamma^{1.5}, \\ e &\propto \gamma^{1}. \end{aligned} \tag{5.3}$$

From these dependencies, a new estimation can be formulated that explicitly includes ω_0. The resulting expression is given in Equation 5.4. For brevity, only the dependence of $\overline{a}$ on ω_0 is shown here (Figures 5.10 to 5.12); the corresponding results for the other coefficients are provided in Appendix C.

$$A_3 = \overline{a}\gamma^{2.25}A_1^5 + \overline{b}\gamma^2 A_1^4 + \overline{c}\gamma A_1^3 + \overline{d}\gamma^{1.5}A_1^2 + \overline{e}\gamma A_1 \tag{5.4}$$

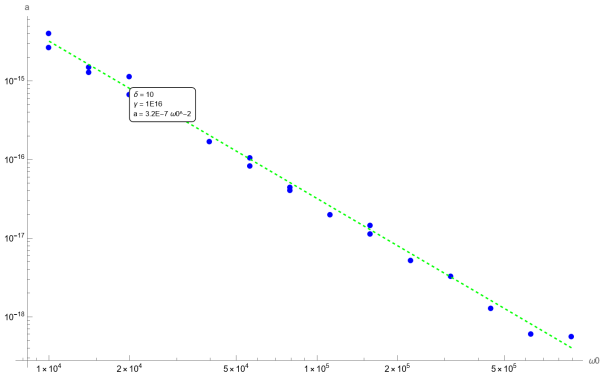

Figure 5.10: $\overline{a}$ as a function of ω_0 at $\gamma = 10^{16}$.

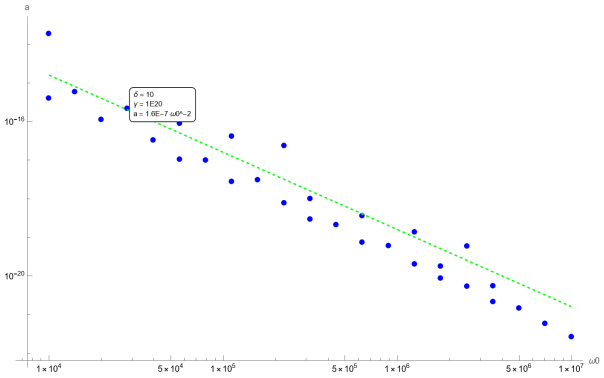

Figure 5.11: $\overline{a}$ as a function of ω_0 at $\gamma = 10^{20}$.

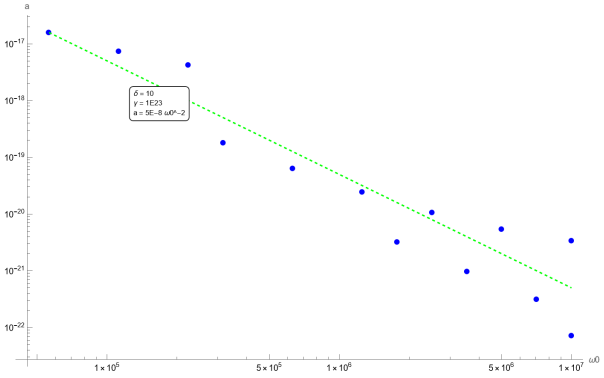

Figure 5.12: $\overline{a}$ as a function of ω_0 at $\gamma = 10^{23}$.

Since γ has already been incorporated into Equation 5.4, the coefficient in front of ω_0 should ideally be constant. Figures 5.10–5.12 show, however, that the coefficient decreases slightly with increasing γ: $3.2 \cdot 10^{-7}$ for $\gamma = 10^{16}$, $1.6 \cdot 10^{-7}$ for $\gamma = 10^{20}$, and $5 \cdot 10^{-8}$ for $\gamma = 10^{23}$. This small variation requires

a correction factor. The general corrected form is given in Equation 5.6, where $\mathcal{C}_n$ denotes correction factors determined from the data.

$$\begin{aligned} \overline{a} &\propto \omega_0^{-2}, \\ \overline{b} &\propto \omega_0^{-2}, \\ \overline{c} &\propto \omega_0^{-1}, \\ \overline{d} &\propto \omega_0^{-1}, \\ \overline{e} &\propto \omega_0^{-1}. \end{aligned} \tag{5.5}$$

$$A_3 = \mathcal{C}_1 \frac{\gamma^{2.25}}{\omega_0^2} A_1^5 + \mathcal{C}_2 \frac{\gamma^2}{\omega_0^2} A_1^4 + \mathcal{C}_3 \frac{\gamma}{\omega_0} A_1^3 + \mathcal{C}_4 \frac{\gamma^{1.5}}{\omega_0} A_1^2 + \mathcal{C}_5 \frac{\gamma}{\omega_0} A_1 \tag{5.6}$$

It was observed that the coefficients for the linear and quadratic terms in the polynomial were extremely small compared to the higher-order terms. This prompted an investigation into whether these contributions could be considered negligible across all examined parameter sets. A second objective was to assess whether the constructed formula accurately reproduces the numerically generated amplitude–amplitude curves, and to identify the ranges of ω_0 and γ for which the approximation remains valid. Representative results for three parameter sets are shown in Figures 5.13 to 5.15, together with the predictions of the constructed equation and the corresponding R^2 values.

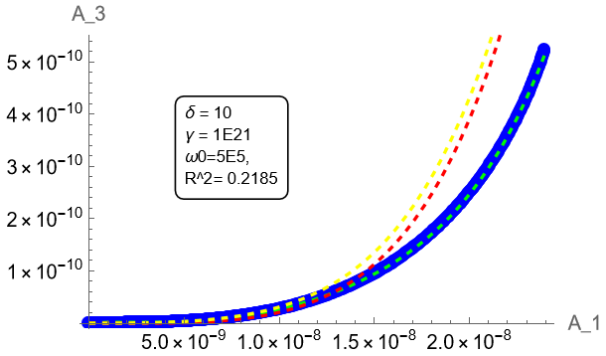

Figure 5.13: Constructed equation compared with numerical results for parameter set 1.

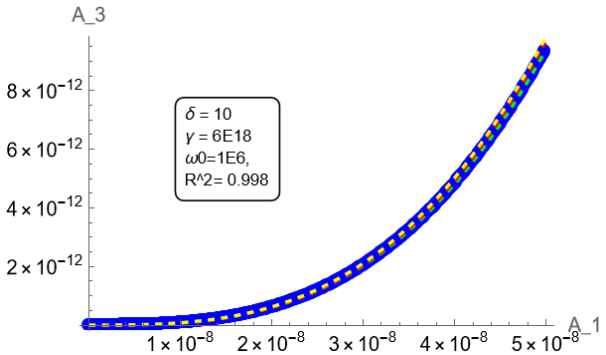

Figure 5.14: Constructed equation compared with numerical results for parameter set 2.

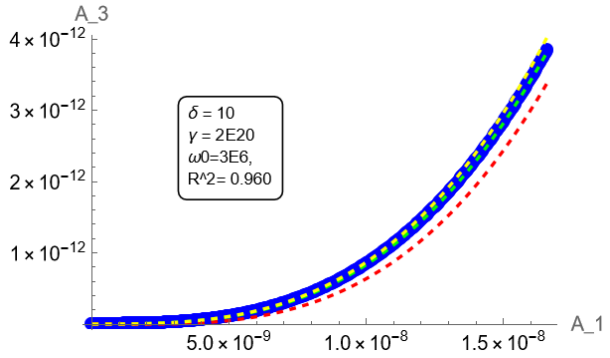

Figure 5.15: Constructed equation compared with numerical results for parameter set 3.

As can be seen, the fits are reasonable but can still be improved. Therefore, the relation in Equation 5.6 was re-tested with numerical data in Mathematica, this time including correction factors to better capture the dependence on γ and ω_0. A new fit was obtained and the variation of the correction factors $\mathcal{C}_1$ to $\mathcal{C}_5$ with γ and ω_0 was determined. The following relations were found:

$$\begin{aligned} \mathcal{C}_1 &= 0.003 \cdot \gamma^{-0.25}, \\ \mathcal{C}_2 &= 8 \cdot 10^{-11}, \\ \mathcal{C}_3 &= 0.013, \\ \mathcal{C}_4 &= 1 \cdot 10^{-21}, \\ \mathcal{C}_5 &= 4 \cdot 10^{-21}. \end{aligned} \tag{5.7}$$

This leads to the final corrected expression:

$$A_3 = 0.003\frac{\gamma^2}{\omega_0^2}A_1^5 + 8 \cdot 10^{-11}\frac{\gamma^2}{\omega_0^2}A_1^4 + 0.013\frac{\gamma}{\omega_0}A_1^3 + 10^{-21}\frac{\gamma^{1.5}}{\omega_0}A_1^2 + 4 \cdot 10^{-21}\frac{\gamma}{\omega_0}A_1. \tag{5.8}$$

Figures 5.16 and 5.17 show the parameter regions where the constructed equation provides a good fit to the numerically generated amplitude–amplitude curves. Figure 5.16 includes both the linear and quadratic terms, whereas Figure 5.17 shows the corresponding results without these small contributions. In both cases, colour indicates the maximum excitation amplitude for which the approximation is valid, according to the legend in Figure 5.18.

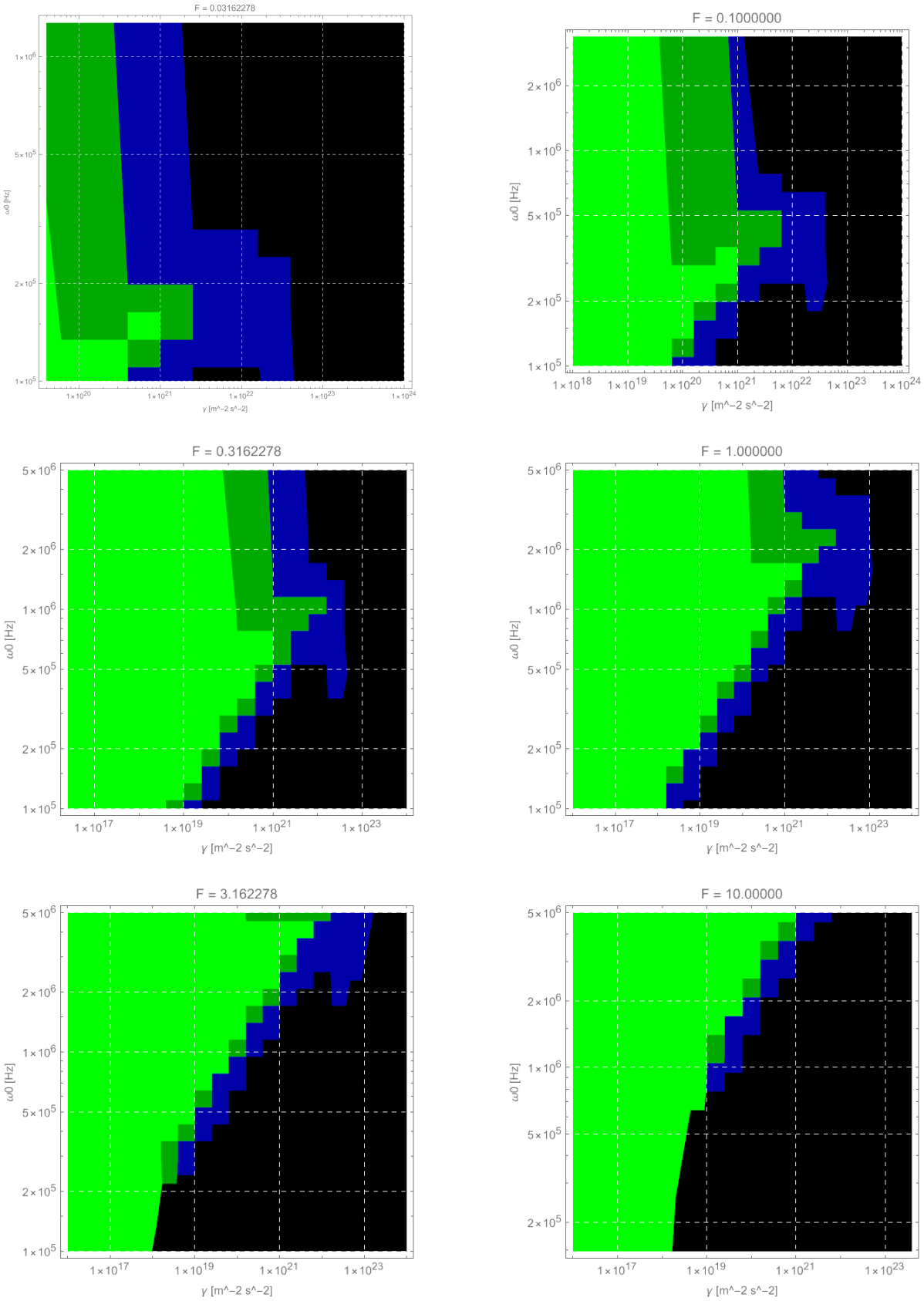

Figure 5.16: Parameter values for which the constructed equation provides a good fit, including linear and quadratic terms.

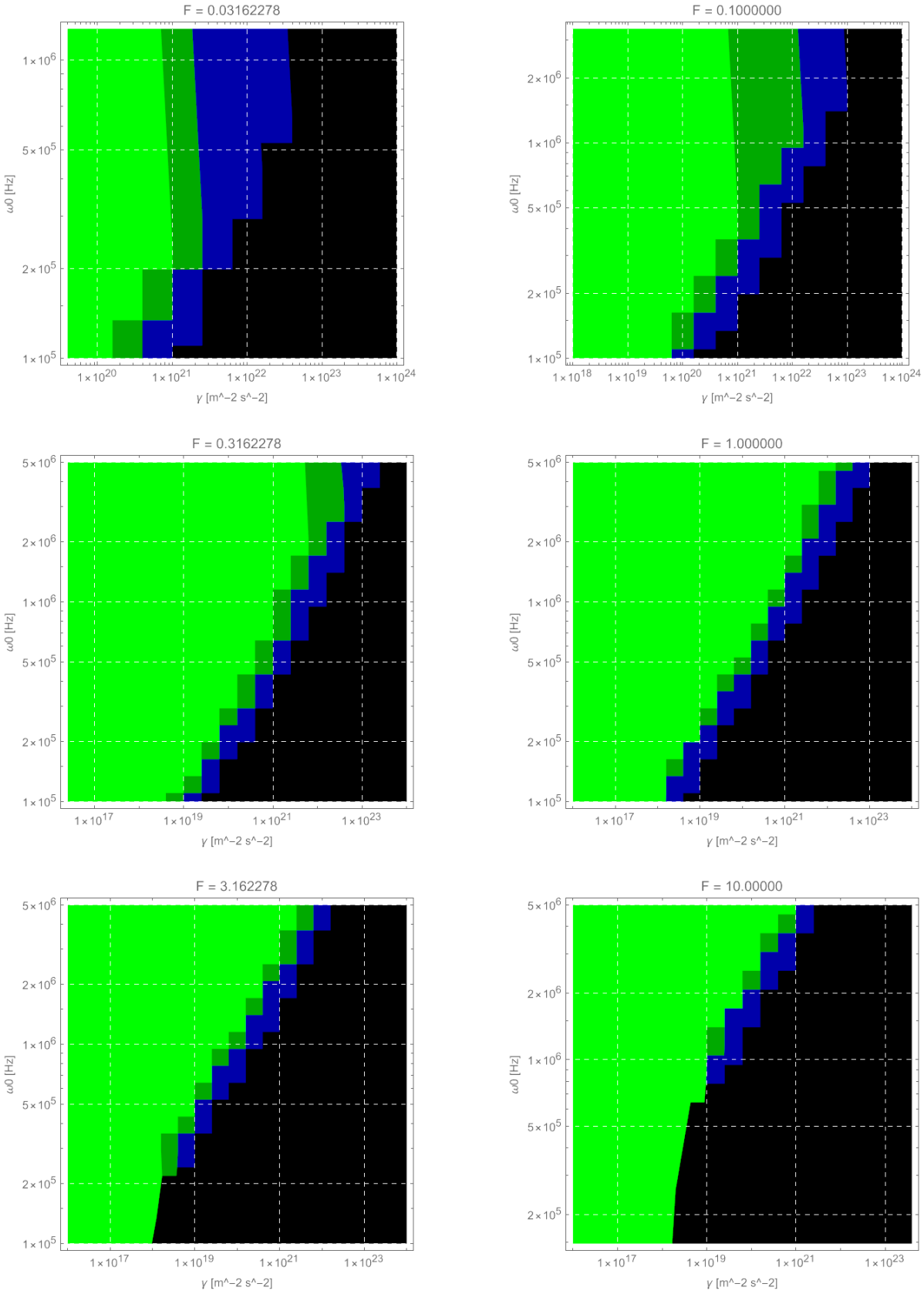

Figure 5.17: Parameter values for which the constructed equation provides a good fit, excluding linear and quadratic terms.

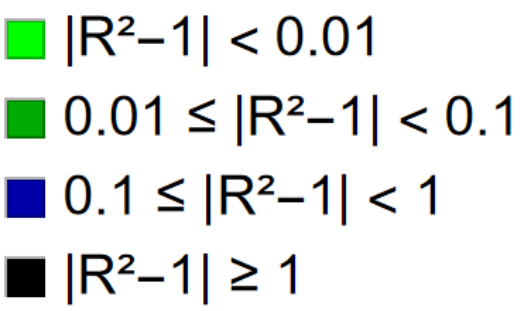

Figure 5.18: Legend for the range indications used in Figures 5.16 and 5.17.

Amplitude Relations in High-Amplitude Regimes

Some systems that exhibit cubic non-linearity do not show dynamic responses in the nanometre regime but instead show micrometre- or even millimetre-scale amplitudes. To simulate such cases in Mathematica, the excitation force had to be increased drastically, in some cases by a factor of $\times 1000$. This introduced several numerical issues: solution branching from third-order polynomials yielding multiple roots, floating-point errors from simultaneously handling very large and very small numbers, and significantly increased computation times.

An alternative approach is to express the relation as a rational function:

$$f(x) = \frac{P(x)}{Q(x)}, \tag{5.9}$$

where $P(x)$ and $Q(x)$ are polynomials. If the degree of $Q(x)$ is n lower than that of $P(x)$, the resulting function will scale as a degree-n polynomial for large x. This asymptotic behaviour corresponds more closely to the analytic relation, and may therefore provide a more robust approximation for high-amplitude regimes.

5.1.3. Comparing the Analytic Solution to Solutions found by Numeric Integration Methods

To further validate the obtained analytical results, a second analysis was performed by directly solving the non-linear differential equation in Equation 2.14 using numerical integration techniques in Python. The integration yields a time-domain solution, which is subsequently transformed into the frequency domain by applying a Direct Fourier Transform (DFT) at the important frequencies. From this, the amplitudes at the excitation frequencies and at the first-order sumfrequencies are extracted. This procedure allows a direct comparison of $A_3(A_1)$ curves with both the harmonic balancing results and the analytic prediction.

For the integration, the explicit RK45 method (Runge–Kutta) was chosen. This algorithm integrates the equation of motion twice—once using a fourth-order Runge–Kutta step and once using a fifth-order step—while using the difference between the two as an error estimate to adapt the step size. Although RK45 is not the most efficient method for stiff or multiscale systems, it provides sufficient accuracy while being less computationally intensive than implicit Runge–Kutta or backward differentiation methods.

From the frequency spectra, the amplitudes at ω_1, ω_2, $\omega_1 - 2\delta$, and $\omega_2 + 2\delta$ were collected into a peak vector. This was repeated for different values of the excitation forces F_1 and F_2. The data enables a systematic comparison of the analytic prediction with direct integration results. To ensure meaningful testing, three parameter sets were chosen based on the validity regions identified in Figure 5.2:

- a set in the green region, where the analytic formula is expected to hold up to 10^{-5} m amplitudes,
- a set in the black region, where the analytic formula is not expected to capture the amplitude–amplitude relation,

- and a set in the blue region, where the analytic relation should be valid only up to moderate excitation forces.

The corresponding results are shown in Figure 5.19. In cases where agreement is expected, the analytic relation closely follows the numerically integrated data. In contrast, for high γ values or parameter sets outside the green region, the analytic relation diverges significantly.

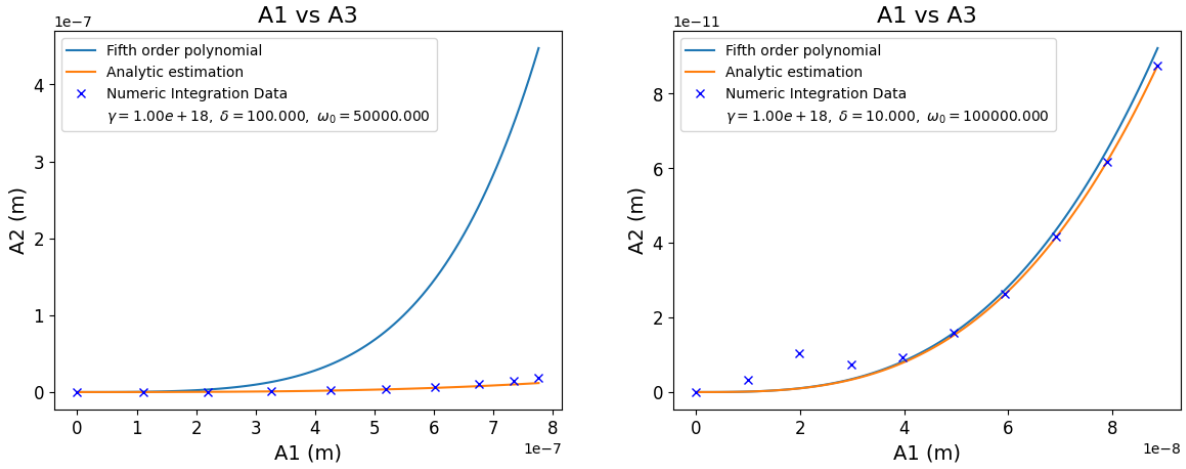

(a) Case 1

(b) Case 2

Figure 5.19: Comparison of numerical integration results with the analytic relation.

At higher values of γ, the solution does not appear to follow a clear A_1–A_3 relation. This effect is shown in Figure 5.20. The symbolic regression solution, although tested, produced values of such large magnitude that it is not displayed here.

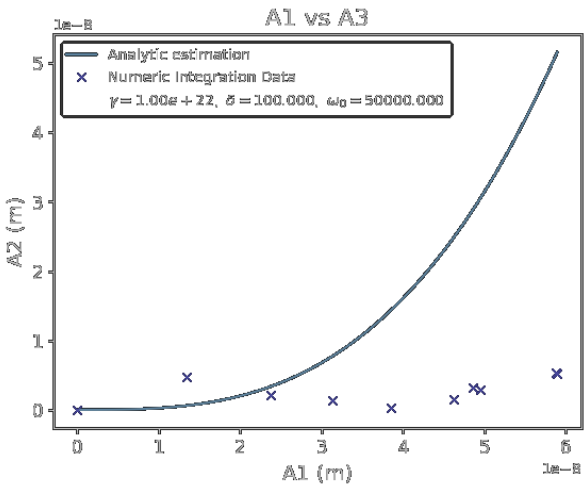

Figure 5.20: Numerical integration results compared to analytic solution at high γ.

A practical challenge of this approach is the required simulation time. A single parameter set can take about one hour to compute accurately, due to the fine time resolution necessary for distinguishing the relevant frequencies. This requirement arises from the ratio between δ and ω_0: the solution combines multiple tones spaced only 2δ apart, producing a slow beating frequency superimposed on the fast oscillations at ω_0. To resolve both time scales, very small time steps and long integration times are required.

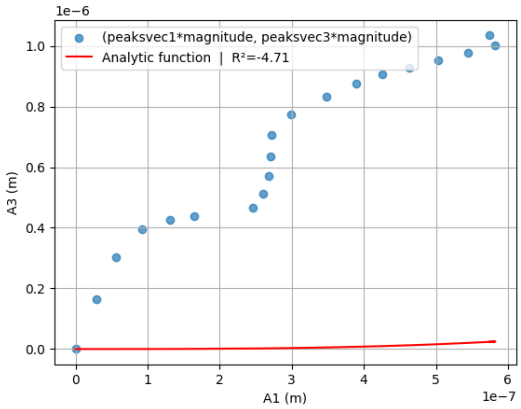

Figure 5.21: Inaccurate results from spectral leakage and data-insufficiency

Furthermore, if too many oscillations are simulated, spectral leakage in the FFT introduces inaccuracies in the extracted amplitudes. To identify an optimal compromise, the influence of the number of slow oscillations was investigated. The test function

$$0.7\cos((1-10^{-5})t) + \cos((1+10^{-5})t) + 0.4\cos((1-3\cdot10^{-5})t) + 0.5\cos((1+3\cdot10^{-5})t)$$

was analysed for different numbers of slow oscillations. As shown in Figure 5.22, ten slow oscillations were sufficient to obtain a clear and stable representation of the relevant amplitudes. This balance between resolution and computational cost was therefore chosen as the target for the numeric solver.

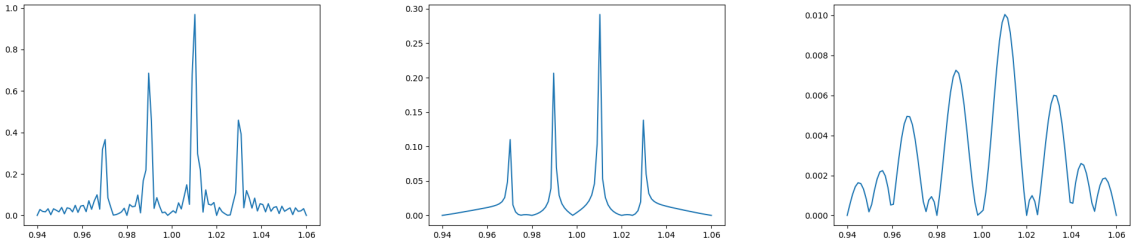

(a) 10 slow oscillations **(b)** 50 slow oscillations **(c)** 200 slow oscillations

Figure 5.22: Comparison of frequency spectra for different numbers of slow oscillations.

It was looked into whether an alternative method of amplitude determination could aid in shortening the calculation time, the result of the methods, the accuracy and the calculation time are presented in the figure below.

In summary, direct numerical integration confirms the trends predicted by the analytic relation in specific regions but also highlights its limitations at higher γ and larger excitation amplitudes. This method provides a benchmark for assessing both the analytic and symbolic regression approaches, albeit at significantly higher computational cost.

5.2. Intermodulation Peaks from Experimental Measurements

5.2.1. Influence of Sample Geometry and Measurement Location

Experimental investigations across multiple samples revealed significant variations in the prominence and distribution of intermodulation peaks. These differences were not only observed between different samples, but also between measurement locations on the same sample. Figures 5.23 and 5.24 illustrate this effect: measurements taken at the centre of a beam produced clearer and more refined intermodulation spectra than measurements at the edges, despite identical excitation conditions.

At first glance, the differences in the ratio between excitation frequencies and intermodulation peaks suggest a non-linear response consistent with the predictions of section 2.4. In theory, increasing excitation force should enhance non-linear interactions, leading to stronger intermodulation products. However, because the applied excitation forces were equal in both cases, the observed discrepancies must be attributed to additional dependencies on geometric and structural factors. Possible influences include beam length, clamping conditions, and local stress distributions.

Comparison between samples further reinforces this claim. For instance, sample 3 exhibited a denser spectrum of intermodulation peaks compared to sample 2, despite the only structural difference being clamping beam length (110 μm vs. 130 μm). This finding highlights the extreme sensitivity of non-linear responses to even small geometric variations.

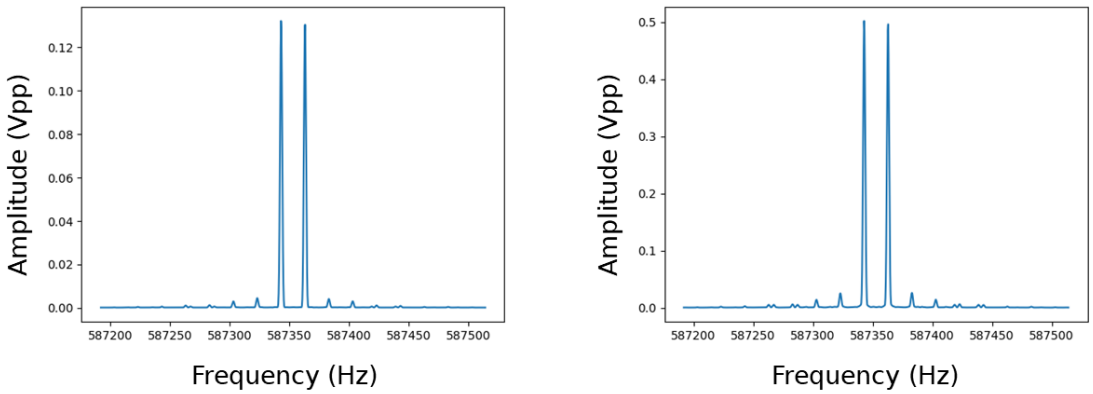

Figure 5.23: Frequency response at the left and middle locations respectively of sample 2 when excited with two tones at resonance.

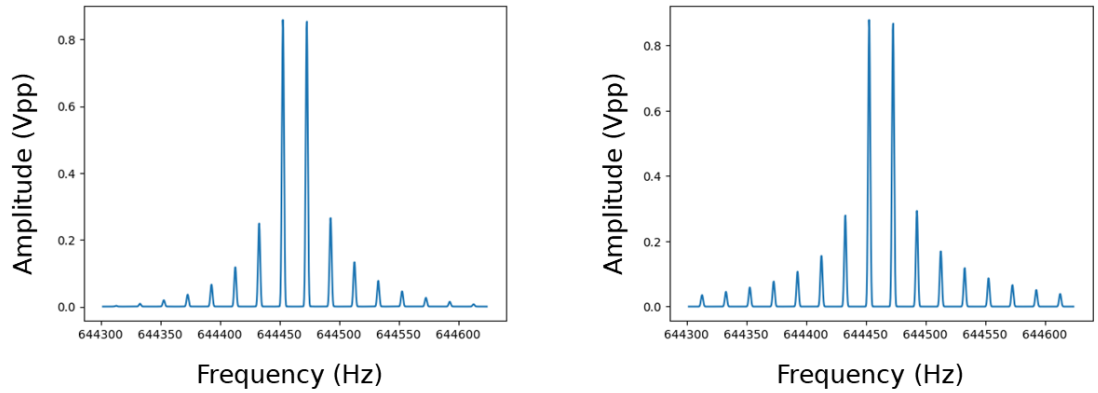

Figure 5.24: Frequency response at the left and middle locations respectively of sample 3 when excited with two tones at resonance.

Additional effects were observed in samples 7 and 9, where the excitation amplitudes at the two fundamental frequencies were highly unequal, despite identical drive voltages. Two explanations are plausible: (i) the excitation was not precisely at resonance, or (ii) the cubic stiffness parameter was relatively small, producing a shallower Duffing response. This interpretation aligns with the simulated Duffing curves in Figure 5.26, where systems with higher cubic stiffness exhibit steeper slopes and larger disparities between the responses at the two excitation frequencies.

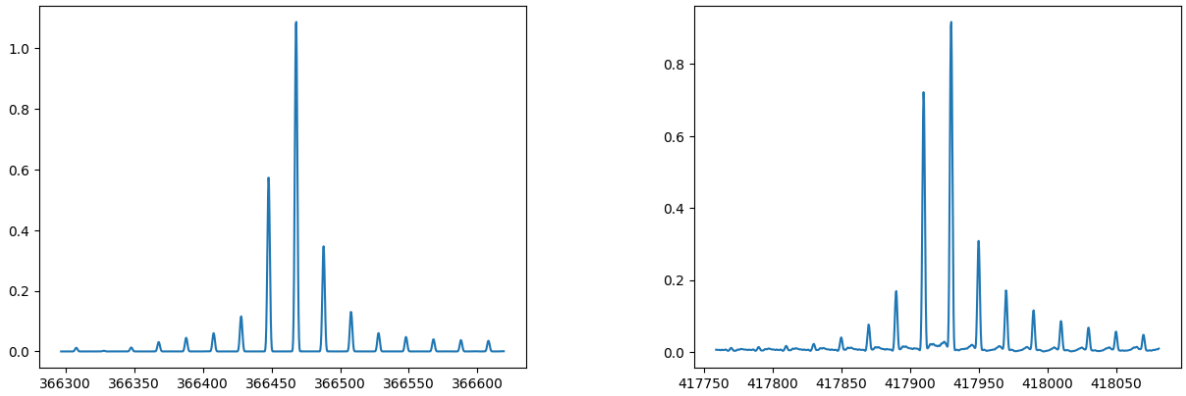

(a) Frequency response in the middle of sample 7

(b) Frequency response in the middle of sample 9

Figure 5.25: Frequency response of samples 7 and 9 when excited with two tones at resonance. Y-axis in Vpp, x-axis in Hz.

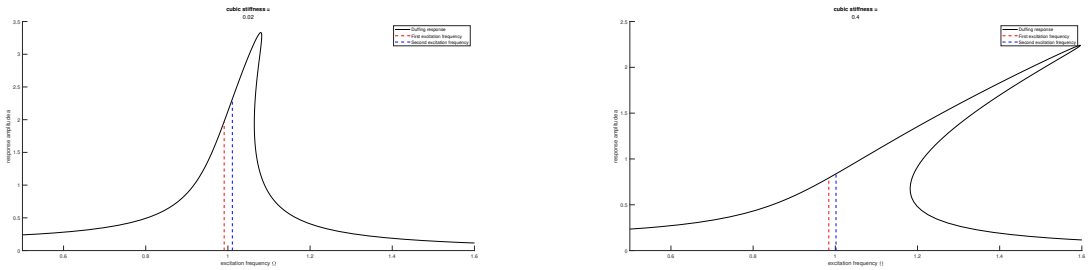

(a) Duffing response with low cubic stiffness

(b) Duffing response with high cubic stiffness

Figure 5.26: Duffing response under two-tone excitation, showing increasing amplitude difference with higher cubic stiffness. Simulated with supplementary code from reference [16]

Overall, these experimental observations demonstrate that non-linear responses in clamped nano-beams are highly sensitive not only to excitation conditions but also to structural and material variations. Even minor changes in geometry, clamping, or measurement position can significantly alter the inter-modulation spectra. This sensitivity must therefore be accounted for when interpreting intermodulation measurements and when attempting to extract quantitative stiffness parameters.

5.3. Validation of Analytic Relations with Experimental Data

To validate the claims made in section 2.4 and subsection 5.1.2, two-tone excitation experiments were performed on clamped nano-beam samples. The analytical relations from subsection 2.4.2 and the numerical results from subsection 5.1.2 are compared against these measurements.

The numerical analysis had predicted that the amplitudes at the excitation frequencies, A_1 and A_2, would relate to each other in an approximately linear fashion. This behaviour was observed both in the analytic solution of the HB-equations and in the direct numerical integration (Figure 5.19). The experimental results confirm this trend, as shown in Figure 5.27. Out of nine measured samples, four displayed consistent behaviour; the remaining samples were excluded due to irregular responses, likely caused by contamination (e.g. dust) on the samples.

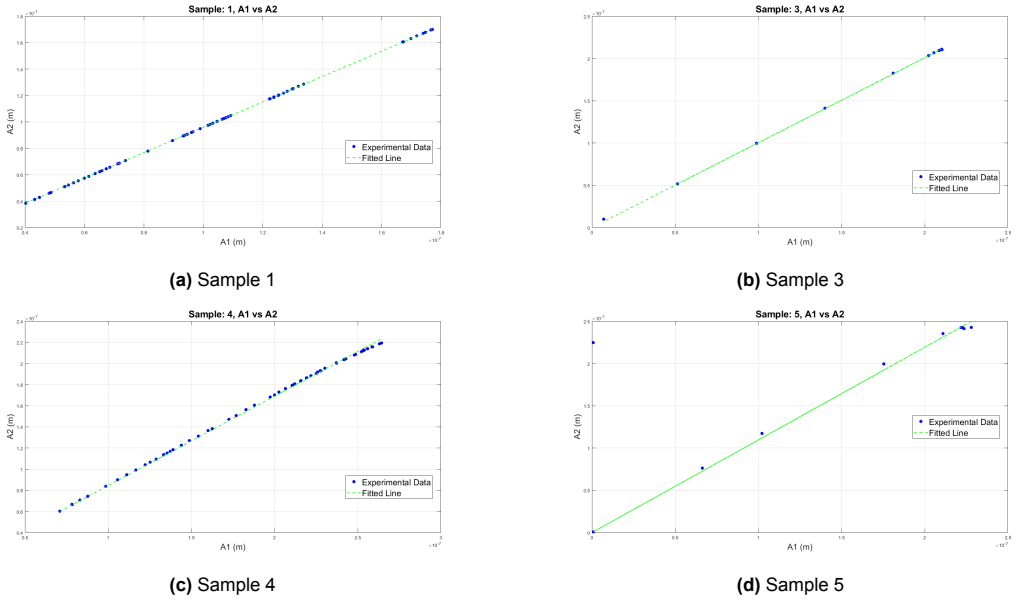

(a) Sample 1 **(b)** Sample 3

(c) Sample 4 **(d)** Sample 5

Figure 5.27: Experimentally determined relations between excitation amplitudes A_1 and A_2. In all four samples, a close-to-linear relation is observed, consistent with theoretical predictions.

5.3.1. Non-linear Cubic Stiffness Estimation

For the four samples showing consistent frequency responses, the data was used to test whether the analytic and symbolic regression relations could be applied to estimate the cubic stiffness parameter γ.

Fitting was performed on the A_1–A_3 relation for each sample. Since the first data points exhibited a constant offset from the x-axis, they were assumed to represent measurement noise. The fit was therefore restricted to the final two-thirds of the data points, where the signal-to-noise ratio was highest.

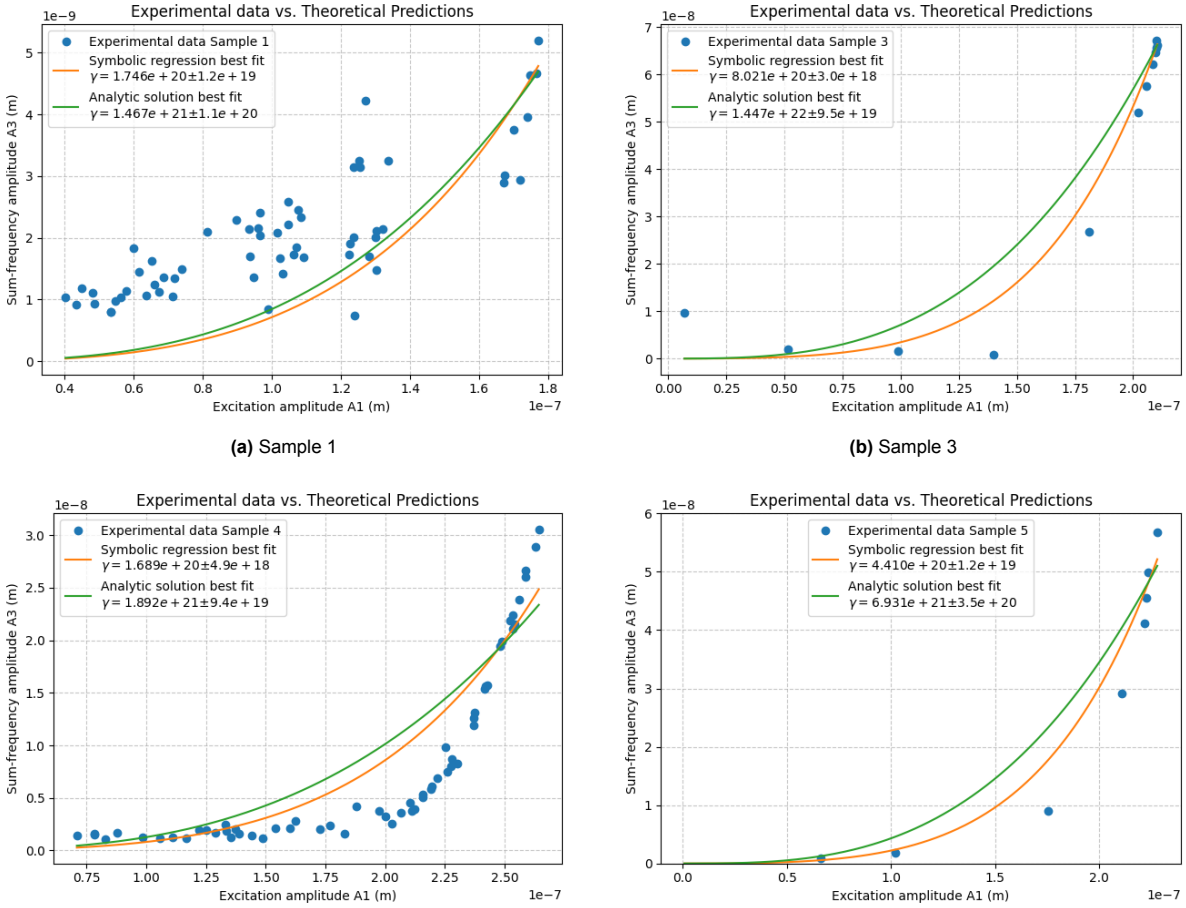

(a) Sample 1

(b) Sample 3

(c) Sample 4

(d) Sample 5

Figure 5.28: Fitting of analytic and symbolic regression relations on experimental data for samples 1, 3, 4, and 5.

Comparing with the previous values of non-linear cubic stiffness of the samples. It can be seen that numbers are not far off but still can be improved on accuracy. The same analytic found function was also tested for these values to see if these values result in a better fit. The result of this can be found in Figure 5.29

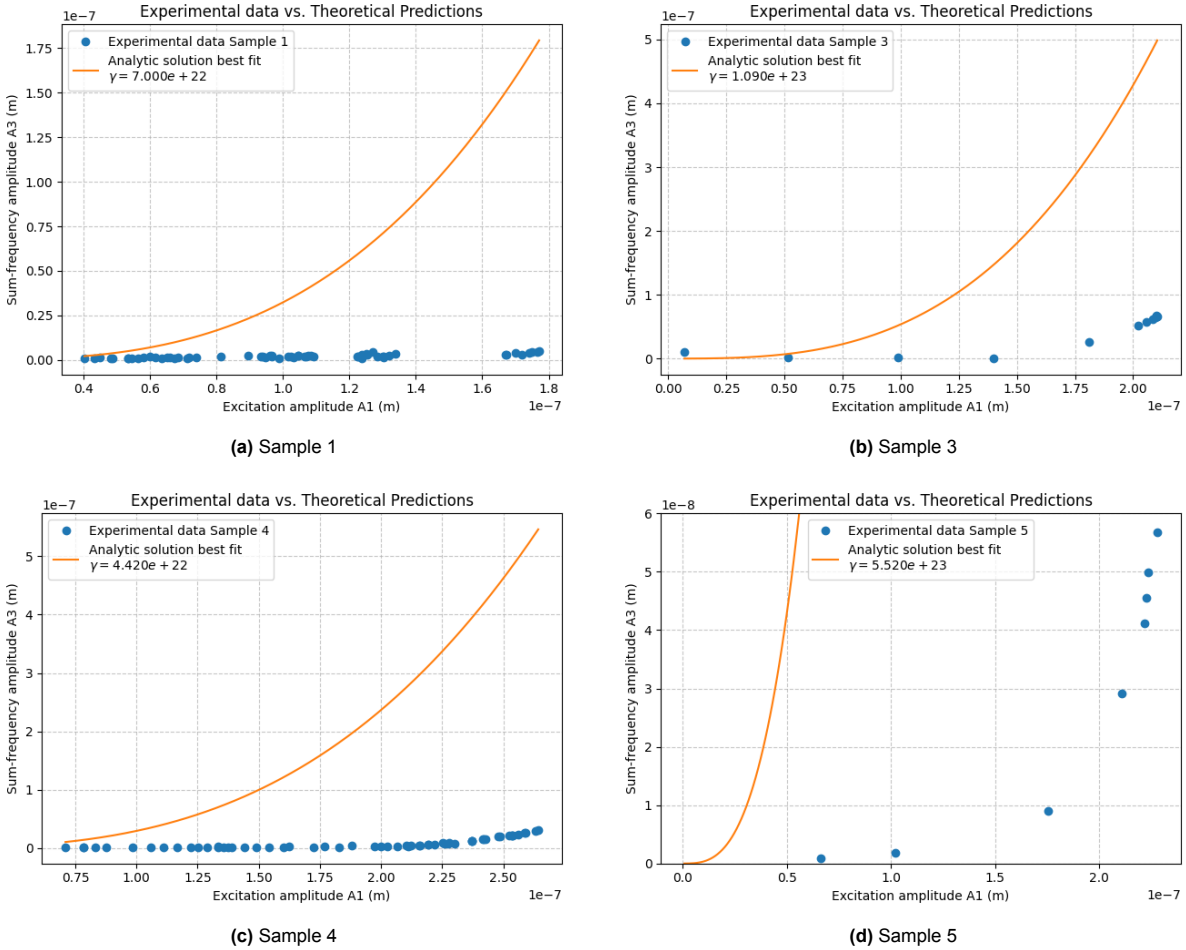

(a) Sample 1

(b) Sample 3

(c) Sample 4

(d) Sample 5

Figure 5.29: Fitting of analytic relation with previously found stiffness on experimental data for samples 1, 3, 4, and 5.

In all four cases (Figure 5.28), both the analytic and symbolic regression fits were applied. While the symbolic regression generally offered better flexibility in reproducing the data trends, neither approach perfectly matched the experimental curves. The experimental A_1–A_3 relations showed a steeper, almost exponential increase with amplitude, deviating from the polynomial behaviour predicted by both theory and numerical simulations. This discrepancy suggests that additional effects—such as higher-order non-linearities, unmodelled damping contributions, or structural imperfections in the samples—may play a significant role in the observed dynamics. For a higher accuracy of modelling, it is suggested to include linear damping, quadratic stiffness and non-linear damping in the harmonic balancing analysis.

Resonance Frequency Shifts Due to Large Excitation

Another observed effect is that the resonance frequency of the clamped beams itself shifts under large excitation forces. This behaviour is typical for non-linear oscillators with cubic stiffness, where the resonance curve bends toward higher or lower frequencies depending on the sign of γ. In practice, this means that as the excitation force is increased, the system no longer oscillates precisely at the small-signal resonance frequency ω_0, but at a shifted resonance frequency ω_{eff}. As a result, both the excitation peaks and the intermodulation products are displaced relative to their theoretical positions. This shift complicates direct comparison with the analytic and numerical predictions, which generally assume a fixed ω_0.

The influence of such resonance shifts may partly explain the exponential-like increase of A_3 observed in Figure 5.28, as the effective detuning becomes smaller with higher excitation. Future work could address this by either explicitly modelling the force-dependent resonance shift in the analytic relation or by applying measurement techniques that track resonance drift during frequency sweeps.

6

Conclusion

The aim of this thesis was to investigate whether intermodulation responses under two-tone excitation can be used to estimate the non-linear stiffness parameters of clamped nano-beams. To address this question, a combined approach was taken: analytic relations were derived using harmonic balancing, numerical solutions were obtained both through symbolic regression and direct time-domain integration, and experimental measurements were carried out on Silicon-Nitride beams using a custom-built setup.

The experimental setup, consisting of a Moku:Lab for signal generation and analysis in combination with a Polytec MSA-500 vibrometer, proved capable of producing accurate and repeatable measurements of intermodulation peaks. Careful validation of the input signals and consideration of non-linearities in auxiliary components ensured that the extracted spectra reflected the behaviour of the clamped beams themselves. This represents a solid experimental foundation on which parameter-estimation methods can be tested.

From the theoretical side, the analytic relation derived between excitation amplitude A_1 and first-order sumfrequency amplitude A_3 was shown to follow the numerical solutions of the harmonic balance equations remarkably well, but only within certain parameter ranges. In particular, the analytic relation remained accurate for low to moderate excitation forces and parameter sets where second-order intermodulation products remain negligible. Outside of these regions, branching of the harmonic balance equations and the onset of neglected higher-order terms caused significant deviations. Symbolic regression was successfully used to extend the applicability, yielding flexible quintic polynomial fits that captured the numerical data across a similar parameter space. Direct numerical integration provided a benchmark, lightly confirming the trends but at the cost of much greater computational effort.

When the analytic and symbolic relations were tested against experimental data, however, no direct quantitative agreement was found. Although the relation between excitation amplitudes A_1 and A_2 was experimentally confirmed to be close to linear, the relation between A_1 and A_3 deviated significantly from theory and simulations. Instead of the predicted polynomial behaviour, the experimental curves displayed a steeper, almost exponential increase with amplitude. This discrepancy suggests that additional physical effects are at play, including resonance frequency shifts under large excitation, higher-order non-linearities, and structural imperfections of the samples. The extreme sensitivity of intermodulation spectra to beam geometry, clamping conditions, and measurement position further complicates direct comparison.

In conclusion, this work demonstrates that:

- A reliable measurement setup was developed and validated for capturing intermodulation responses of nano-beam resonators under two-tone excitation.
- The analytic relation obtained from harmonic balancing is valid within a well-defined parameter range and accurately predicts numerical solutions in those regimes.

- Symbolic regression extends this validity by providing accurate data-driven relations, though at the expense of interpretability.
- Experimental results qualitatively confirm non-linear behaviour but do not quantitatively correlate with the analytic or numerical relations, indicating that the theoretical model is incomplete for describing the real system.

The thesis thus highlights both the potential and the limitations of using intermodulation products in combination with harmonic balancing for parameter estimation in non-linear resonators.

7

Discussion

7.1. Theory

The analytic framework developed in this thesis was based on harmonic balancing with simplifying assumptions, including neglecting certain higher-order terms and assuming equal excitation amplitudes. Within restricted parameter regimes, this approach was shown to reproduce numerical solutions well. However, outside these ranges the analytic relation diverged due to multiple solution branches in the harmonic balance equations and the influence of second-order intermodulation products.

Symbolic regression was introduced as a way to extend validity and capture amplitude–amplitude relations more flexibly. While this method produced accurate fits across a wider parameter space, the resulting expressions lack the interpretability of the analytic solution. Moreover, they do not provide direct physical insight into how non-linear parameters such as γ influence the system.

One key limitation of the theoretical approach is the exclusion of damping effects and higher-order non-linearities. In practice, the dynamics of clamped beams are influenced not only by cubic stiffness but also by additional non-linearities (quadratic terms, non-linear damping) and by resonance frequency shifts under strong excitation. Incorporating these effects into the analytic model would make the expressions more complex but also more representative of experimental behaviour.

As to why the experimental data shows exponential growth of the first order sumfrequency amplitudes: It could have multiple reasons.

A first presumption is that the order of approximation is not defined well enough. When the order of approximation is expanded, the resulting analytic relation will be a polynomial which includes higher degrees of A_1. When a Taylor expansion is done on an exponential function it is able to be approximated by a polynomial of infinite degree. Therefore the found relation could be seen as exponential.

A second presumption is an inaccuracy in measurements. When measuring the amplitude of a MEMS-sample while increasing the excitation force it was assumed that the input and output voltages linearly correspond to the amplitude of the sample. This is excluding the input and output non-linearities that could possibly be prevented by using predistortion.

A third presumption is that there is missing theory on the topic of two-tone excitation responses of a system with non-linear stiffness. There are already some studies on the possible reasons of sudden changes in behaviour when exciting a system with duffing non-linearity at different force levels and possible bifurcations, changes in stable points, due to this increase in excitation. [6] [4] [17]. An example of this can be seen in Figure 7.1, which is the result of a measurement that was recently done by one of the supervisors that shows the behaviour of sumfrequency amplitudes over excitation force. Therefore it is difficult to exactly describe the relation between excitation amplitude and any sumfrequency amplitude with one simple equation.

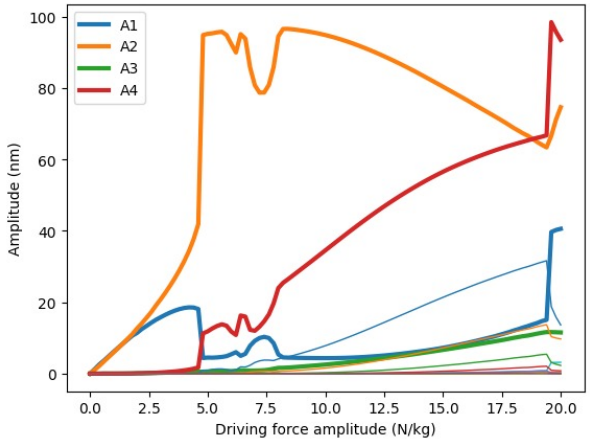

Figure 7.1: Numerical simulation of intermodulation product amplitudes over excitation force

7.2. Experiments

The experimental setup was capable of producing accurate measurements of intermodulation spectra, yet several limitations were identified that may have influenced the results:

- The Moku:Lab device was used both to generate and to receive signals. This dual use could introduce feedback or artefacts that are difficult to isolate from the actual system response.
- Attenuation was caused by long connecting wires, which introduced additional resistance. Shorter, low-resistance cabling is recommended to minimise this effect.
- A lock-in amplifier could have been employed, particularly for samples with higher resonance frequencies, to extract weak frequency components from noisy spectra.
- The Laser Doppler Vibrometer (LDV) output velocity data, which was then processed by the spectrum analyser. This means that the analysis was based on velocity rather than displacement, potentially introducing a scaling mismatch with the theoretical model, which assumes displacement.

In addition, experimental inconsistencies such as dust contamination on samples and small differences in beam geometry (length, clamping, buckling angle) were observed to have significant effects on the measured intermodulation peaks. These factors, combined with the non-linearities already present in the signal chain (power combiner, amplifier), complicate direct validation of the theoretical relations.

7.3. Recommendations for Future Work

Experiments

Future experiments should focus on reducing non-linearities in the setup itself. This includes verifying the linearity of the input signals with external equipment, using low-loss cabling, and incorporating a lock-in detection scheme for cleaner amplitude extraction. Improved sample handling (e.g. avoiding dust contamination) and resonance tracking during frequency sweeps would also reduce uncertainty in the results.

Theory

From the theoretical side, several improvements are possible:

- Employ a more complete ansatz that includes damping and higher-order non-linearities. Although this will complicate the analytic relations, it could provide better alignment with experimental data. The reason such extensions were not pursued in this thesis was to maintain tractability of the equations and focus on cubic stiffness.
- Consider alternative methods such as the method of averaging, which may simplify the derivation of approximate relations while still capturing essential non-linear effects.
- Investigate the use of envelope detection in the time domain instead of FFT-based frequency

extraction. This could reduce computation time and help resolve small frequency differences more efficiently.

- The effects of two tone excitation bring several complexities with it that can not be explained yet. first, a better method to describe behaviour under two tone excitation needs to be studied.

Overall, the work presented in this thesis provides a foundation for testing analytic models of non-linear stiffness estimation. Future studies should combine improved experimental setups with extended theoretical models to further explain the difference between simulations and measurements and make estimating non-linear stiffness with two-tone excitation possible.

8

Acknowledgements

First I want to thank Peter Steeneken for assigning me this great thesis project. Then I want to thank Farbod Alijani for taking over guidance halfway through the project and picking up supervising when Peter was less available, even though Farbod was very busy with his many master students already. The supervision and guidance was always critical and rightly so. Sometimes Farbod would say things that I had completely missed but were very straightforward and other times give insights I could not even dream to come up with. The knowledge about non-linear dynamics Farbod has is something I look up to with much respect and awe. These insights and this large amount of knowledge was also present in the mind of Chris Wattjes who I want to thank sincerely for the great guidance and great availability. I wish him the best of luck with acquiring his doctorate.

I also want to thank Zichao Li for the samples, LDV tutorials and always openness to talk about theory and experiments. It was also very interesting to be present at his PhD thesis defence.

Next, I want to thank Raymond Knetemann for his ultra refined code to run numeric integration quickly. Lastly, Thanks to all the members of the NCANTO Group meetings for insights. I hope all your projects will turn out great.

ChatGPT was used as aid for writing code and improving readability of the report but not for generating new information. It was used according to the AI-guidelines of the PME-department of the TU Delft.

References

[1] Luis A. Aguirre and Christophe Letellier. “Modeling Nonlinear Dynamics and Chaos: A Review”. In: *Mathematical Problems in Engineering* 2009.1 (2009), p. 238960. DOI: https://doi.org/10.1155/2009/238960. eprint: https://onlinelibrary.wiley.com/doi/pdf/10.1155/2009/238960. URL: https://onlinelibrary.wiley.com/doi/abs/10.1155/2009/238960.

[2] Farbod Alijani, Zichao Li, and Minxing Xu et al. “Strain Engineering of Nonlinear Nanoresonators from Hardening to Softening”. In: (Oct. 2023). PREPRINT (Version 1) available at Research Square. URL: https://doi.org/10.21203/rs.3.rs-3344257/v1.

[3] Mahmoud Alizadeh and Daniel Rönnow. “A two-tone test for characterizing nonlinear dynamic effects of radio frequency amplifiers in different amplitude regions”. In: *Measurement* 89 (2016), pp. 273–279. ISSN: 0263-2241. DOI: https://doi.org/10.1016/j.measurement.2016.04.027. URL: https://www.sciencedirect.com/science/article/pii/S026322411630094X.

[4] Adriano A. Batista and A. A. Lisboa de Souza. “Frequency-comb response of a parametrically driven Duffing oscillator to a small added ac excitation”. In: *Journal of Applied Physics* 128.24 (Dec. 2020). ISSN: 1089-7550. DOI: 10.1063/5.0029104. URL: http://dx.doi.org/10.1063/5.0029104.

[5] Vincent Bos. “Nonlinear dynamics of graphene membranes”. In: (2020). URL: https://resolver.tudelft.nl/uuid:7ddd6ce3-831c-4ae3-96b3-9dc5bb5079bd.

[6] Letizia Catalini et al. “Slow and fast topological dynamical phase transitions in a Duffing resonator driven by two detuned tones”. In: *Physical Review Research* 7.3 (July 2025). ISSN: 2643-1564. DOI: 10.1103/y9gq-yjxy. URL: http://dx.doi.org/10.1103/y9gq-yjxy.

[7] Animesh Chatterjee. “Parameter estimation of Duffing oscillator using Volterra series and multi-tone excitation”. In: *International Journal of Mechanical Sciences* 52.12 (2010), pp. 1716–1722. ISSN: 0020-7403. DOI: https://doi.org/10.1016/j.ijmecsci.2010.09.005. URL: https://www.sciencedirect.com/science/article/pii/S002074031000216X.

[8] Animesh Chatterjee and Nalinaksh Vyas. “Non-linear parameter estimation with Volterra series using the method of recursive iteration through harmonic probing”. In: *Journal of Sound and Vibration* 268 (Dec. 2003), pp. 657–678. DOI: 10.1016/S0022-460X(02)01537-7.

[9] C.J. Clark et al. “Power-amplifier characterization using a two-tone measurement technique”. In: *Microwave Theory and Techniques, IEEE Transactions on* 50 (July 2002), pp. 1590–1602. DOI: 10.1109/TMTT.2002.1006421.

[10] Robin J. Dolleman et al. “Graphene Squeeze-Film Pressure Sensors”. In: *Nano Letters* 16.1 (2016). PMID: 26695136, pp. 568–571. DOI: 10.1021/acs.nanolett.5b04251. eprint: https://doi.org/10.1021/acs.nanolett.5b04251. URL: https://doi.org/10.1021/acs.nanolett.5b04251.

[11] Selcuk Oguz Erbil et al. “Full Electrostatic Control of Nanomechanical Buckling”. In: *Phys. Rev. Lett.* 124 (4 Jan. 2020), p. 046101. DOI: 10.1103/PhysRevLett.124.046101. URL: https://link.aps.org/doi/10.1103/PhysRevLett.124.046101.

[12] Samer Houri et al. “Pulse-width modulated oscillations in a nonlinear resonator under two-tone driving as a means for MEMS sensor readout”. In: *Japanese Journal of Applied Physics* 58.SB (Feb. 2019), SBBI05. ISSN: 1347-4065. DOI: 10.7567/1347-4065/aaffb9. URL: http://dx.doi.org/10.7567/1347-4065/aaffb9.

[13] Liquid Instruments. *Moku:Lab Specifications*. Accessed: 2025-03-14. 2024. URL: https://download.liquidinstruments.com/documentation/specs/hardware/mokulab/MokuLab-Specifications.pdf.

[14] Ata Ke şkekler et al. “Multimode Nonlinear Dynamics of Graphene Resonators”. In: *Phys. Rev. Appl.* 20 (6 Dec. 2023), p. 064020. DOI: 10.1103/PhysRevApplied.20.064020. URL: https://link.aps.org/doi/10.1103/PhysRevApplied.20.064020.

[15] Ata Keşkekler et al. “Multimode Nonlinear Dynamics of Graphene Resonators”. In: *Phys. Rev. Appl.* 20 (6 Dec. 2023), p. 064020. DOI: 10.1103/PhysRevApplied.20.064020. URL: https://link.aps.org/doi/10.1103/PhysRevApplied.20.064020.

[16] Malte Krack and Johann Gross. *Harmonic Balance for Nonlinear Vibration Problems*. Mathematical Engineering. Springer International Publishing, Cham, 2019. DOI: 10.1007/978-3-030-14023-6.

[17] Péter Krähling et al. “Attractor selection in nonlinear oscillators by temporary dual-frequency driving”. In: *Nonlinear Dynamics* 111.20 (2023), pp. 19209–19224. ISSN: 1573-269X. DOI: 10.1007/s11071-023-08855-3. URL: https://doi.org/10.1007/s11071-023-08855-3.

[18] Mingchen Lv et al. “Design and Optimization of MEMS Resonant Pressure Sensors with Wide Range and High Sensitivity Based on BP and NSGA-II”. In: *Micromachines* 15.4 (2024). ISSN: 2072-666X. DOI: 10.3390/mi15040509. URL: https://www.mdpi.com/2072-666X/15/4/509.

[19] Ali H. Nayfeh and Dean T. Mook. *Nonlinear Oscillations*. 1st. Vol. 22. Pure and Applied Mathematics. New York: John Wiley & Sons, 1979, pp. xiv + 704.

[20] Gert Roebben, Corneliu Sarbu, and Omer Van der Biest. “High□temperature stiffness and damping to qualitatively assess the amorphous intergranular phase in sintered silicon nitride and carbide”. In: *Journal of the European Ceramic Society* 23.13 (2003), pp. 2037–2045. DOI: 10.1016/S0955-2219(03)00105-4.

[21] Banafsheh Sajadi et al. “Nonlinear dynamic identification of graphene’s elastic modulus via reduced order modeling of atomistic simulations”. In: *Journal of the Mechanics and Physics of Solids* 122 (2019), pp. 161–176. ISSN: 0022-5096. DOI: https://doi.org/10.1016/j.jmps.2018.09.013. URL: https://www.sciencedirect.com/science/article/pii/S0022509618305180.

[22] Dong Hoon Shin et al. “Graphene nano-electromechanical mass sensor with high resolution at room temperature”. In: *iScience* 26.2 (2023), p. 105958. ISSN: 2589-0042. DOI: https://doi.org/10.1016/j.isci.2023.105958. URL: https://www.sciencedirect.com/science/article/pii/S2589004223000354.

[23] Chris F. D. Wattjes. “Experimental parameter estimation of nonlinear stiffness using multi-tone excitation”. Master’s thesis. Delft University of Technology, 2024.

[24] Mohammad I. Younis, Fadi Alsaleem, and Daniel Jordy. “The response of clamped–clamped microbeams under mechanical shock”. In: *International Journal of Non-Linear Mechanics* 42.4 (2007). Special Issue Micro-and Nanoscale Beam Dynamics, pp. 643–657. ISSN: 0020-7462. DOI: https://doi.org/10.1016/j.ijnonlinmec.2007.01.017. URL: https://www.sciencedirect.com/science/article/pii/S0020746207000480.

[25] Bowei Zhang et al. “Novel two-tone measurement of the nonlinearity and memory effects of mixers in different amplitude regions of large carrier signals”. In: *Review of Scientific Instruments* 92.12 (Dec. 2021), p. 124710. ISSN: 0034-6748. DOI: 10.1063/5.0058668. eprint: https://pubs.aip.org/aip/rsi/article-pdf/doi/10.1063/5.0058668/16137058/124710_1_online.pdf. URL: https://doi.org/10.1063/5.0058668.

[26] Ya Zhang et al. “Giant Enhancement in the Thermal Responsivity of Microelectromechanical Resonators by Internal Mode Coupling”. In: *Physical Review Applied* 14.1 (July 2020). ISSN: 2331-7019. DOI: 10.1103/physrevapplied.14.014019. URL: http://dx.doi.org/10.1103/PhysRevApplied.14.014019.

A

Python, Matlab and Mathematica code used

Due to the large amount of code, a google drive link is supplied where all of the following scripts can be found:

`https://drive.google.com/drive/folders/1maRdTGqyokbCXVsgQDJKGnQGxAFMNEUW?usp=drive_link`

A description of what every file does is supplied in Table A.1 below.

Mathematica	
File	**Description**
HB Parameterless.nb	Perform analytic Harmonic balancing, generating equations. Solving these equations numerically and perform Symbolic regression on the generated curves Find regions of parameter sets where the symbolic regression accurately follows the numerical solutions.
HB parameterlessestimateequations.nb	Perform analytic Harmonic balancing Generate analytic relation by analytic solving of resulting equations with assumptions Solving resulting equations numerically Find regions of parameter sets where the analytic relations accurately follows the numerical solutions

Table A.1: Mathematica files description

MATLAB	
File	**Description**
forcesweeps_to_get_relations.m	Import all experimental data and sort it into frequency data and amplitude data. Use this to visualise in 3d how the peaks evolve over input force.

Python	
File	**Description**
Extract data from Matlab and fit	Extract the data that was sorted in MATLAB to fit with analytic relatio
Intermodulation ROM-Multi Mode	Used to generate artificial data using numeric integration, Written by
Function analysis	Used to investigate the analytic relation as function of the input para
Forcerelation obtainment single sumfrequency	Used to measure at a set frequency when exciting with two tones

B

Sample properties and manual for reconstructing experiments

The samples were kept in a constant vacuum of $1.2 \cdot 10^{-8}$ bar.

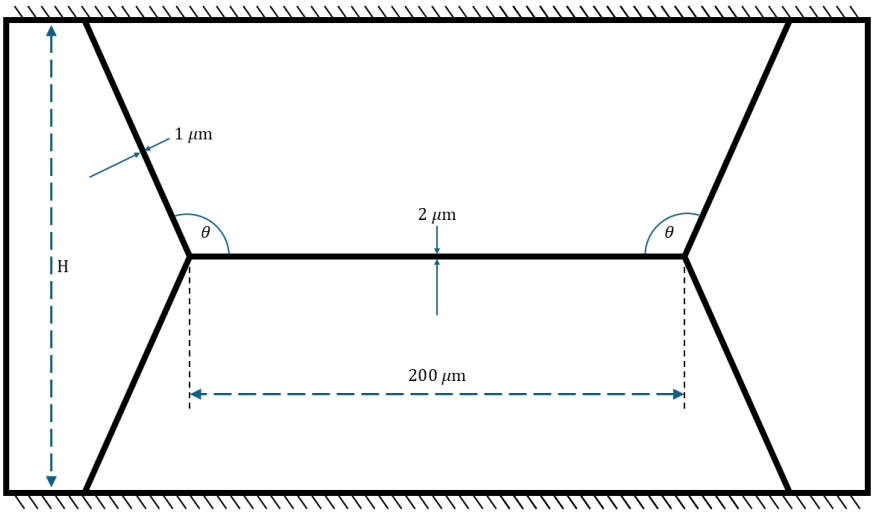

Figure B.1: Example of a sample

Sample	Resonance (kHz)	Clamping Length H (μm)	θ (degrees)	γ ($s^{-2}m^{-2}$)
1	549.7	150	107	$7{,}00 \cdot 10^{22}$
2	587.4	130	107	$8{,}57 \cdot 10^{22}$
3	644.5	110	107	$1{,}09 \cdot 10^{23}$
4	473.1	150	101	$4{,}42 \cdot 10^{22}$
5	509.7	130	101	$5{,}52 \cdot 10^{23}$
6	- -	110	101	$6{,}91 \cdot 10^{22}$
7	366.3	150	95	$1{,}64 \cdot 10^{22}$
8	392.1	130	95	$2{,}25 \cdot 10^{22}$
9	417.9	110	95	$3{,}02 \cdot 10^{22}$

B.1. Manual for finding Intermodulation peaks using described setup

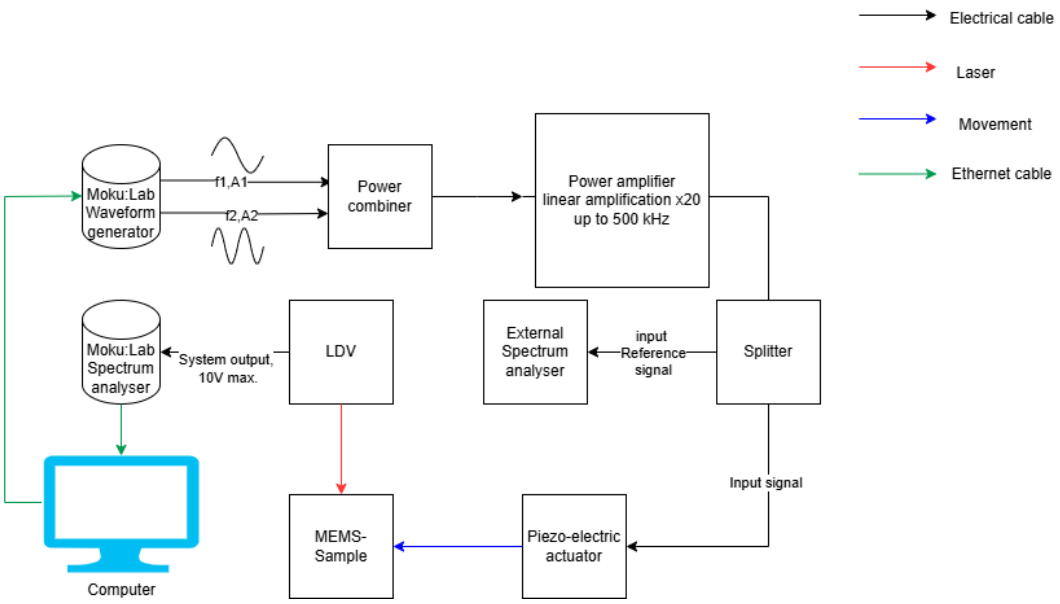

Figure B.2: Used setup for measurements

This manual describes the procedure for reproducing the measurements as outlined in Figure B.2 A slightly modified version of this setup was also tested, in which a band-pass filter was applied to reduce artifacts in the input signals at the second and third harmonic of the input frequency. In that configuration, a Zurich Instruments Lock-in amplifier generated the signals, and the Moku:Lab was used to apply a band-pass filter. The procedure below refers to the standard setup and assumes the experiments are to be done in the cleanroom at the faculty of Mechanical Engineering in TU Delft and that the Polytec MSA-500 LDV is used.

Step-by-Step Procedure

1. **Preparation in the cleanroom:** Enter the cleanroom while adhering to all regulations. Ensure that the samples remain free from dust or other contaminants that could change the dynamics of the sample and thus interfere with measurements.
2. **Powering devices:** Turn on the following equipment in order: Computer (The one connected to the LDV), Vibrometer controller, Junction Box, and Moku:Lab. Additionally, prepare a personal device with ethernet or Wi-Fi connection (e.g., laptop) to run the control code on. **Important:** Do *not* turn on the amplifier on at this stage to avoid voltage surges that could damage the devices.
3. **Connecting devices:** Wire the system according to Figure B.2. Verify that all cables, splitters, and combiners are properly connected and functioning. In the past, a situation has occured where one of the splitters was not functioning properly and generated electrical non-linearities on its own. Due to this, the input signal showed a frequency comb at the input frequencies already.
4. **Connecting Moku:Lab:** Establish a connection between the Moku:Lab and the control device via Ethernet (preferred) or Wi-Fi.
5. **Configuring the LDV:** Launch the Polytec Analyzer application on the PC. Adjust the LDV lens focus and align the laser spot on the sample surface. It is recommended to target a location where the vibration amplitude is relatively low, as large displacements in the z-direction may cause the laser to defocus. It is thus also recommended to watch the laser signal strength during excitation to ensure it remains constant.
6. **Running the experiment code:** Execute the script corresponding to the desired measurement. Monitor the LDV output indicator to ensure that the input signal does not exceed the operational range.
7. **Verifying signal integrity:** Using an external spectrum analyzer (in this study, the Polytec system itself), confirm that the input consists of a clean linear combination of two tones. Ensure that no artifacts or harmonic artifacts appear in the frequency range of interest.
8. **Finishing or repeating measurements:** Once the experiment is complete, turn off the signal generator. If additional measurements are required, reposition the sample using the 2-DoF stage under the Polytec MSA-500, or safely disconnect the setup.

C

Symbolic regression

C.1. Coefficient scaling determination

b,

for b, the absolute data was plotted. b can be negative.

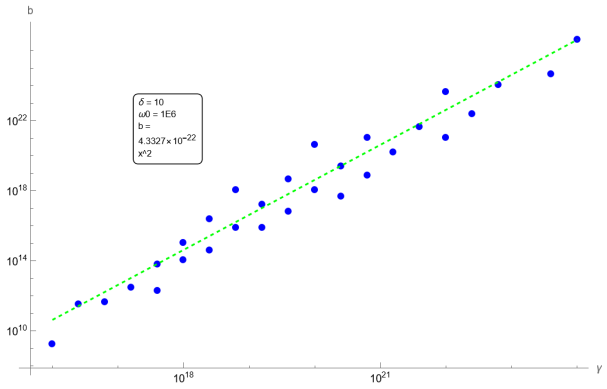

Figure C.1: b as function of γ

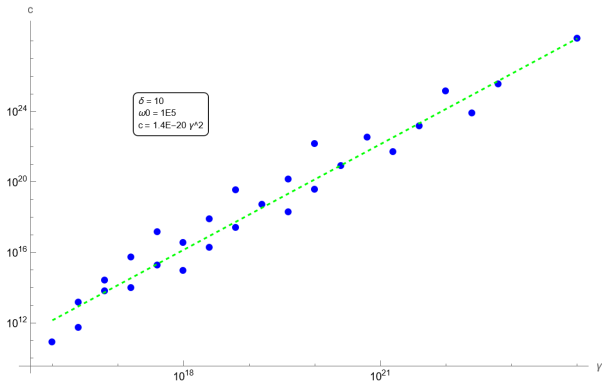

Figure C.2: b as function of γ

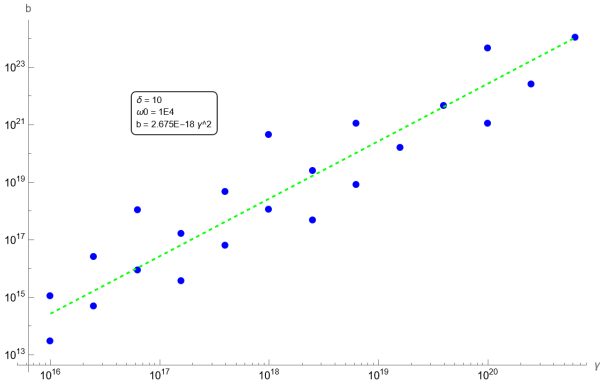

Figure C.3: b as function of γ

c

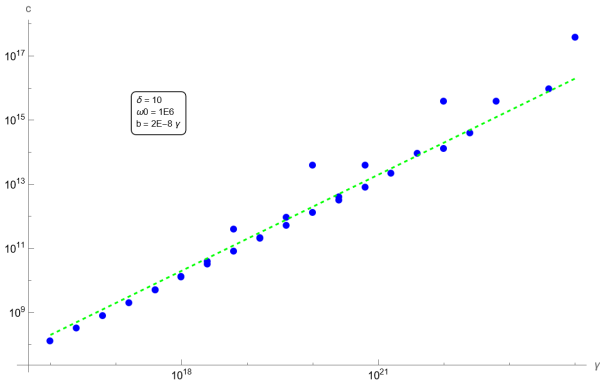

Figure C.4: c as function of γ

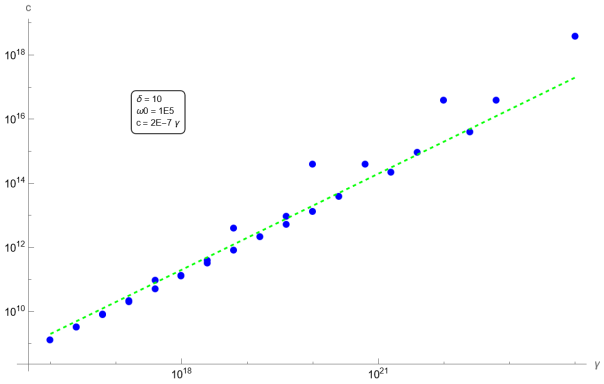

Figure C.5: c as function of γ

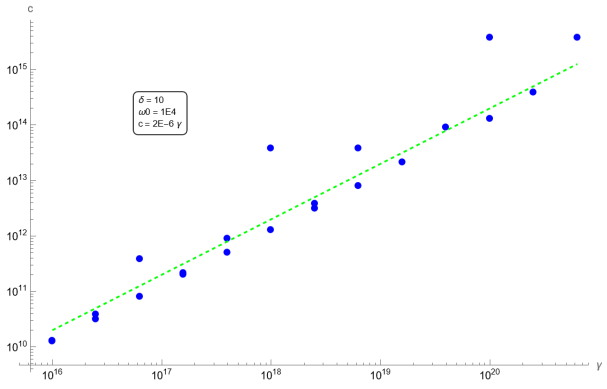

Figure C.6: c as function of γ

d

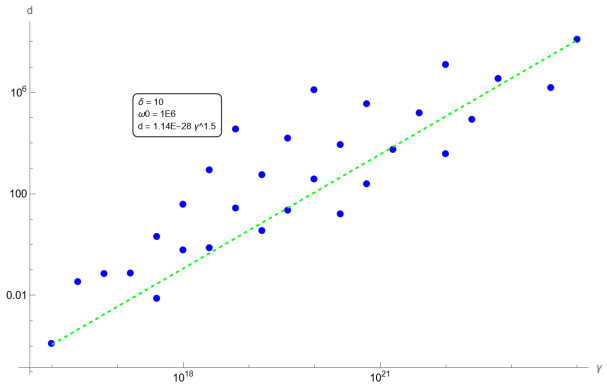

Figure C.7: d as a function of γ

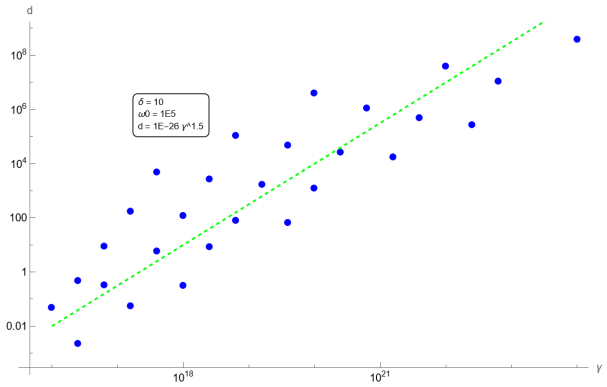

Figure C.8: d as function of γ

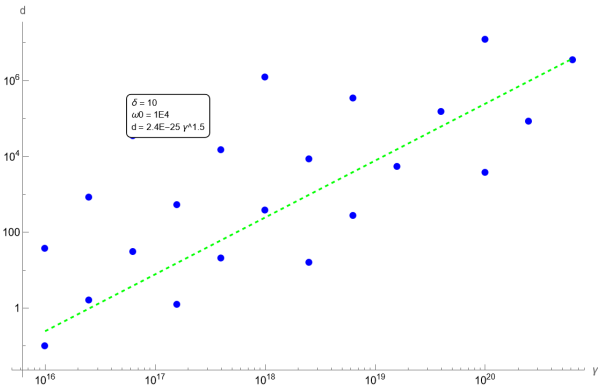

Figure C.9: d as function of γ

e

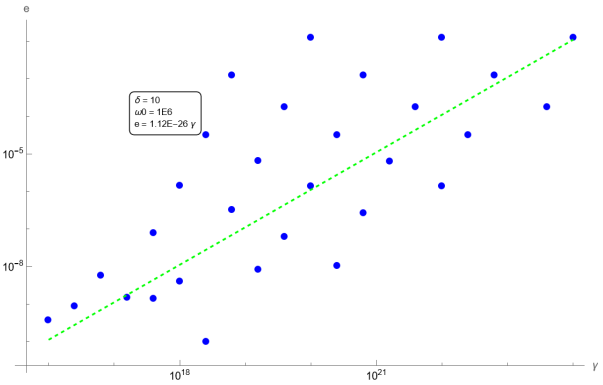

Figure C.10: e as function of γ

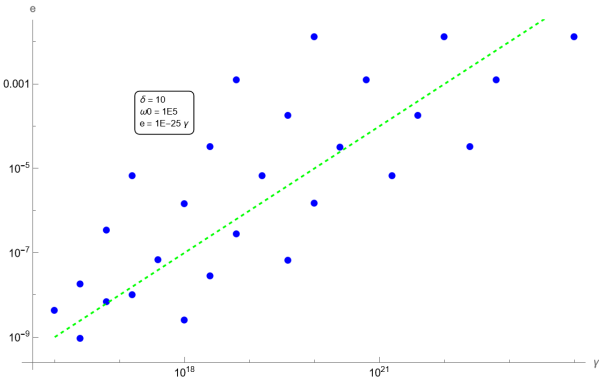

Figure C.11: e as function of γ

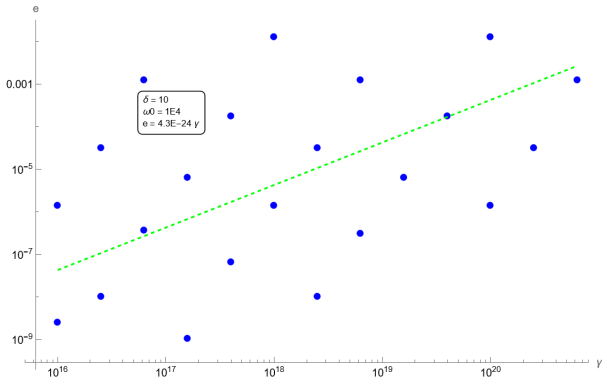

Figure C.12: e as function of γ

Omega sweeps

C.2. second iteration of coefficients determination

$\overline{b}$

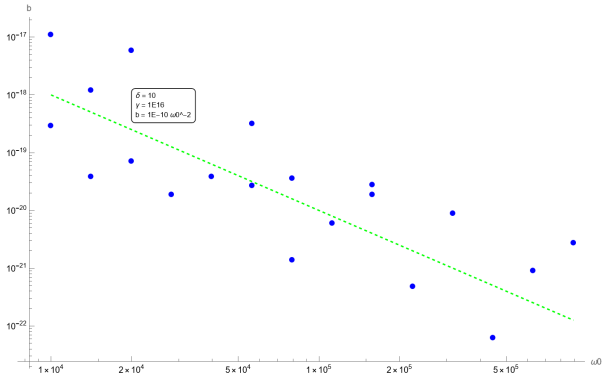

Figure C.13: $\overline{b}$ as a function of ω_0

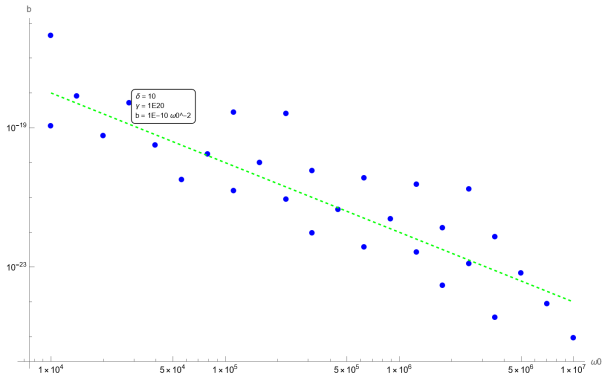

Figure C.14: $\overline{b}$ as a function of ω_0

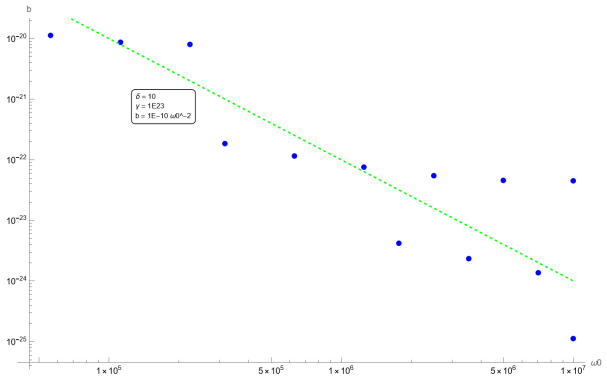

Figure C.15: $\overline{b}$ as a function of ω_0

b does not need a correction factor, the coefficient is 1E-10.

$\overline{c}$

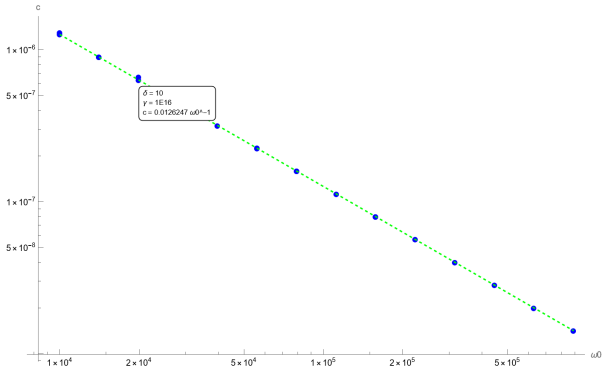

Figure C.16: $\overline{c}$ as a function of ω_0

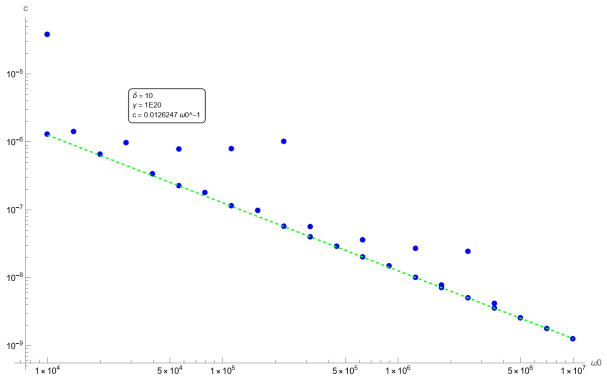

Figure C.17: $\overline{c}$ as a function of ω_0

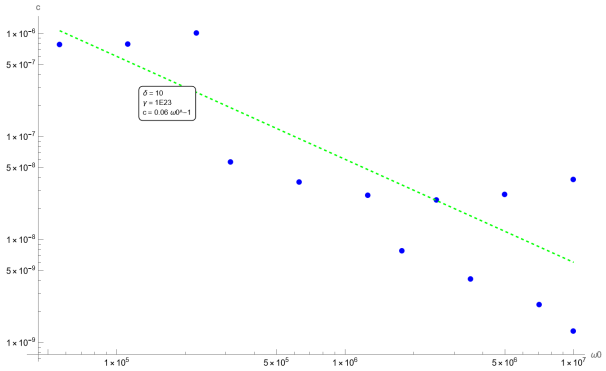

Figure C.18: $\overline{c}$ as a function of ω_0

c does not need a correction factor. d

d is often negative

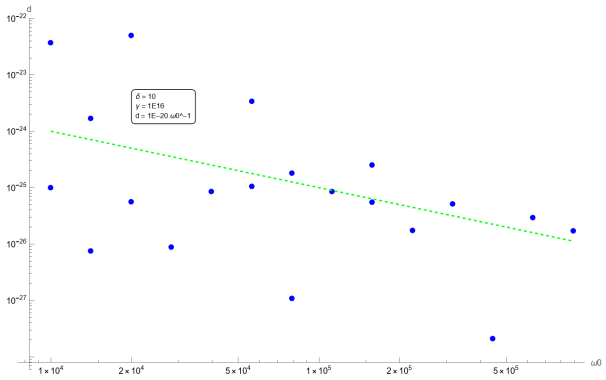

Figure C.19: $\overline{d}$ as a function of ω_0

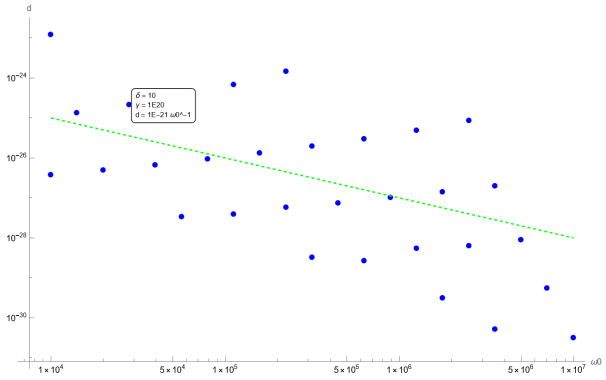

Figure C.20: $\overline{d}$ as a function of ω_0

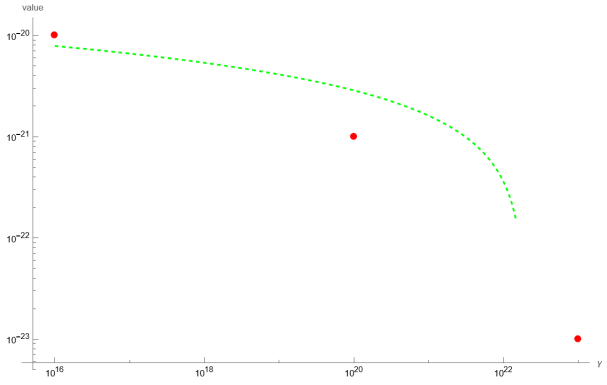

Figure C.22: correction factor determination for d

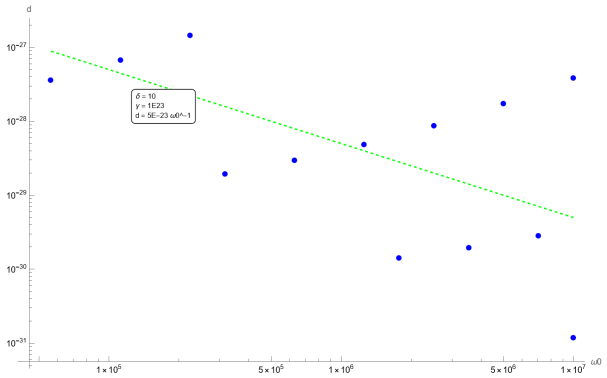

Figure C.21: $\overline{d}$ as a function of ω_0

e

e is sometimes negative

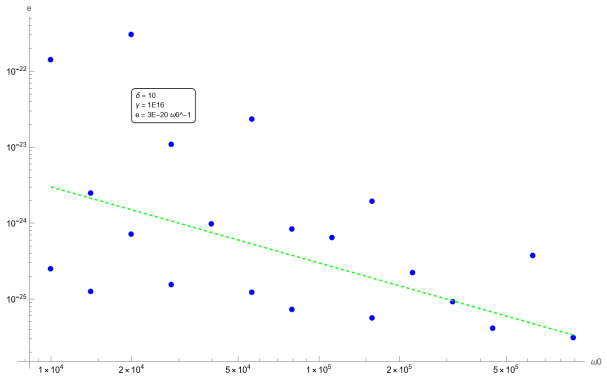

Figure C.23: $\overline{e}$ as a function of ω_0

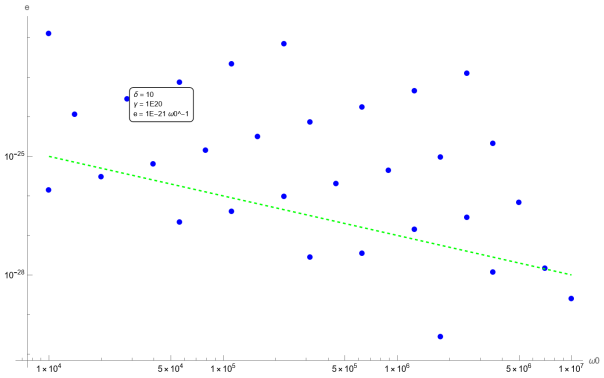

Figure C.24: $\overline{e}$ as a function of ω_0

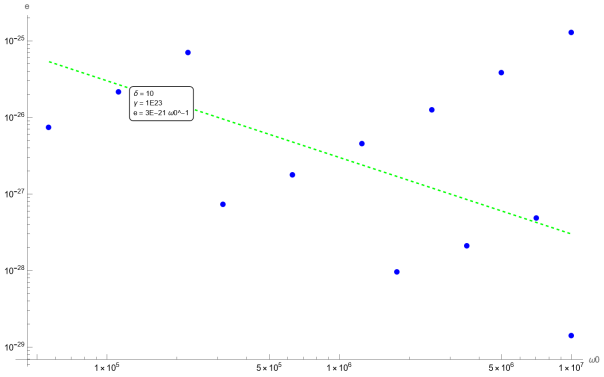

Figure C.25: $\overline{e}$ as a function of ω_0

D

Determination of analytic relation between A_1 and A_3

The harmonic balancing method is applied by introducing an ansatz of the form shown in Equation D.1.

$$\begin{aligned} y(t) = {} & A_1 \cos(\omega_1 t) + A_2 \cos(\omega_2 t) \\ & + A_3 \cos\big((2\omega_1 - \omega_2)t\big) + A_4 \cos\big((\omega_1 - 2\omega_2)t\big) \\ & + A_5 \cos(3\omega_1 t) + A_6 \cos(3\omega_2 t) \\ & + A_7 \cos\big((3\omega_1 - 2\omega_2)t\big) + A_8 \cos\big((2\omega_1 - 3\omega_2)t\big). \end{aligned} \tag{D.1}$$

This ansatz includes the excitation frequencies, the third harmonics, and the first- and second-order sum frequencies. Substituting this expression for $y(t)$ into the equation of motion in Equation D.2 yields the relations that will be considered in the derivation of a relation between A_1 and A_3.

$$\ddot{y}(t) + \omega_0^2 y(t) + \gamma y^3(t) = f_1 \cos(\omega_1 t) + f_2 \cos(\omega_2 t). \tag{D.2}$$

Since A_3 corresponds to the amplitude of $\cos\big((2\omega_1 - \omega_2)t\big)$, the coefficients of this frequency component are collected and equated to zero. The resulting equation is:

$$\begin{aligned} & \tfrac{3}{4}A_1^2 A_2 \gamma + \tfrac{3}{2}A_1^2 A_3 \gamma + \tfrac{3}{2}A_2^2 A_3 \gamma + \tfrac{3}{4}A_3^3 \gamma + \tfrac{3}{2}A_1 A_2 A_4 \gamma + \tfrac{3}{2}A_3 A_4^2 \gamma \\ & + \tfrac{3}{2}A_1 A_2 A_5 \gamma + \tfrac{3}{2}A_3 A_4 A_5 \gamma + \tfrac{3}{2}A_3 A_5^2 \gamma + \tfrac{3}{4}A_4^2 A_6 \gamma + \tfrac{3}{2}A_4 A_5 A_6 \gamma + \tfrac{3}{2}A_3 A_6^2 \gamma \\ & + \tfrac{3}{2}A_1 A_2 A_7 \gamma + \tfrac{3}{2}A_1 A_3 A_7 \gamma + \tfrac{3}{2}A_2 A_4 A_7 \gamma + \tfrac{3}{2}A_3 A_7^2 \gamma + \tfrac{3}{4}A_2^2 A_8 \gamma + \tfrac{3}{2}A_1 A_4 A_8 \gamma \\ & + \tfrac{3}{2}A_2 A_6 A_8 \gamma + \tfrac{3}{2}A_4 A_7 A_8 \gamma + \tfrac{3}{2}A_5 A_7 A_8 \gamma + \tfrac{3}{2}A_3 A_8^2 \gamma + A_3 \omega_0^2 - 4A_3 \omega_1^2 \\ & + 4A_3 \omega_1 \omega_2 - A_3 \omega_2^2 = 0. \end{aligned} \tag{D.3}$$

In order to express A_3 solely as a function of A_1, the remaining amplitudes must be eliminated. For this, the following assumptions are introduced:

1. $\omega_1 = \omega_0 - \delta$.
2. $\omega_2 = \omega_0 + \delta$.
3. $A_7 = A_8 = 0$.
4. $A_1 = A_2$.
5. A_5 and A_6 are given by the relations in Equation 2.24.

Assumptions 1 and 2 introduce the detuning parameter δ, allowing the influence hereof to be examined. Assumption 3 neglects the terms A_7 and A_8, which are typically very small and have a negligible effect on A_3. Assumption 4 approximates A_1 and A_2 as equal, consistent with their near-identical amplitudes in practice. The resulting reduced equation is presented in Equation D.4.

$$\begin{aligned} & \tfrac{3}{4}A_1^3 \gamma + 3A_1^2 A_3 \gamma + \tfrac{3}{4}A_3^3 \gamma + A_3 \omega_0^2 - 4A_3 \big(-\delta + \omega_0\big)^2 \\ & + 4A_3 \big(-\delta + \omega_0\big)\big(\delta + \omega_0\big) - A_3 \big(\delta + \omega_0\big)^2 \\ & + \frac{3A_1^6 A_3 \gamma^3}{32\big(\omega_0^2 - 9(-\delta + \omega_0)^2\big)^2} - \frac{3A_1^5 \gamma^2}{8\big(\omega_0^2 - 9(-\delta + \omega_0)^2\big)} \\ & + \frac{3A_1^6 A_3 \gamma^3}{32\big(\omega_0^2 - 9(\delta + \omega_0)^2\big)^2} = 0. \end{aligned} \tag{D.4}$$

Although this equation can in principle be solved analytically, the resulting expression is significantly lengthy and not included here for the sake of simplicity. To further simplify, the method of ordering coefficients is applied. Retaining only terms of total order six leads to the reduced equation in Equation D.5, and the resulting explicit relation for $A_3(A_1)$ is given in Equation D.6.

$$\begin{aligned}&\tfrac{3}{4}A_1^3\gamma + 3A_1^2A_3\gamma + A_3\omega_0^2 - 4A_3\big(-\delta+\omega_0\big)^2\\&+ 4A_3\big(-\delta+\omega_0\big)\big(\delta+\omega_0\big) - A_3\big(\delta+\omega_0\big)^2\\&- \frac{3A_1^5\gamma^2}{8\big(\omega_0^2 - 9(-\delta+\omega_0)^2\big)} = 0\end{aligned} \tag{D.5}$$

$$A_3 = \frac{-A_1^5\gamma^2 - 18A_1^3\gamma\delta^2 + 36A_1^3\gamma\delta\omega_0 - 16A_1^3\gamma\omega_0^2}{8\big(A_1^2\gamma - 3\delta^2 + 2\delta\omega_0\big)\big(9\delta^2 - 18\delta\omega_0 + 8\omega_0^2\big)}. \tag{D.6}$$

Assumption 4, namely $A_1 = A_2$, can be questioned. While experimental results show that in certain cases the amplitudes at the excitation frequencies are indeed equal, in other cases their magnitudes differ by up to a factor of two. Two representative examples are shown in Figure D.1.

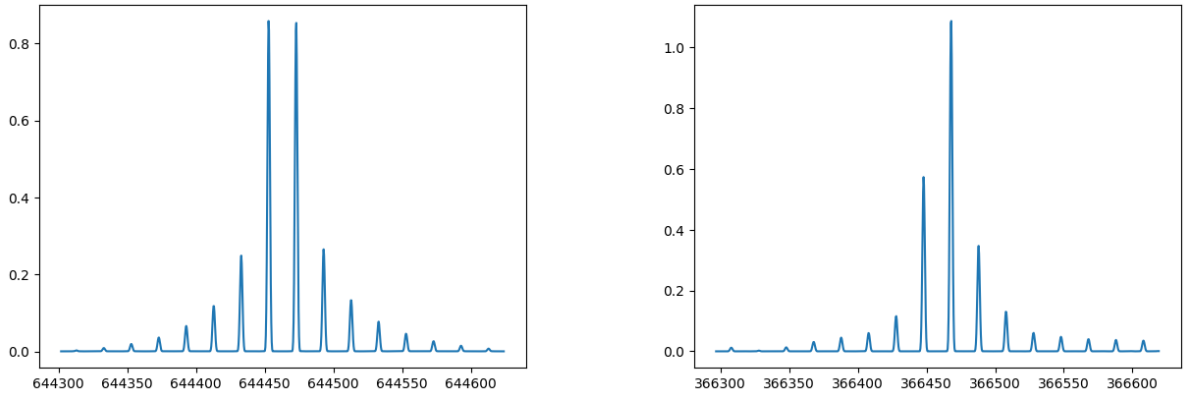

(a) Frequency response on the left side of sample 3.

(b) Frequency response in the middle of sample 3.

Figure D.1: Examples illustrating that the excitation amplitudes A_1 and A_2 are not always equal in practice.

To address this, an analytic relation between A_1 and A_2 is sought. This is achieved by applying harmonic balancing to the coefficients of $\cos(\omega_1 t)$. Collecting the relevant terms yields Equation D.7, which depends on A_2^6 and consequently has six possible roots that cannot be expressed in simple analytic form. To obtain a simpler expression, the equation is reduced to coefficients of up to third order, giving Equation D.8. Solving this relation yields $A_2(A_1)$, shown in Equation D.9.

$$\begin{aligned}&-2F_1 + \frac{3A_1^3\gamma}{2} + 3A_1A_2^2\gamma + 2A_1\omega_0^2 - 2A_1(-\delta+\omega_0)^2\\&+ \frac{3A_1^7\gamma^3}{16\big(\omega_0^2 - 9(-\delta+\omega_0)^2\big)^2} - \frac{3A_1^5\gamma^2}{8\big(\omega_0^2 - 9(-\delta+\omega_0)^2\big)}\\&+ \frac{3A_1A_2^6\gamma^3}{16\big(\omega_0^2 - 9(\delta+\omega_0)^2\big)^2} = 0\end{aligned} \tag{D.7}$$

$$-2F_1 + \frac{3A_1^3\gamma}{2} + 3A_1A_2^2\gamma + 2A_1\omega_0^2 - 2A_1(-\delta+\omega_0)^2 = 0 \tag{D.8}$$

$$A_2 = \sqrt{\frac{4F_1}{6\gamma A_1} - \tfrac{1}{2}A_1^2 + \tfrac{2}{3}\frac{\delta}{\gamma}(\delta - 2\omega_0)}. \tag{D.9}$$

Substituting this relation for A_2 results in the following revised set of assumptions:

1. $\omega_1 = \omega_0 - \delta$.
2. $\omega_2 = \omega_0 + \delta$.
3. $A_7 = A_8 = 0$.
4. $A_2 = -\sqrt{\frac{4F_1}{6\gamma A_1} - \frac{1}{2}A_1^2 + \frac{2}{3}\frac{\delta}{\gamma}(\delta - 2\omega_0)}$.
5. A_5 and A_6 are given by the relations in Equation 2.24.

With these revised assumptions, a new equation is obtained by collecting the coefficients of $\cos((2\omega_1 - \omega_2)t)$ and equating them to zero:

$$\begin{aligned}
&\tfrac{3}{2}A_1^2 A_3\gamma - \tfrac{1}{4}\sqrt{\tfrac{3}{2}}\,A_1^{3/2}\sqrt{\gamma}\sqrt{4F_1 - 3A_1^3\gamma + 4A_1\delta(\delta - 2\omega_0)} \\
&\quad + \frac{A_3\big(4F_1 - 3A_1^3\gamma + 4A_1\delta(\delta - 2\omega_0)\big)}{4A_1} + A_3\omega_0^2 \\
&\quad - 4A_3(-\delta + \omega_0)^2 + 4A_3(-\delta + \omega_0)(\delta + \omega_0) - A_3(\delta + \omega_0)^2 \\
&\quad + \frac{\sqrt{\tfrac{3}{2}}\,A_1^{7/2}\gamma^{3/2}\sqrt{4F_1 - 3A_1^3\gamma + 4A_1\delta(\delta - 2\omega_0)}}{8\big(\omega_0^2 - 9(-\delta + \omega_0)^2\big)} \\
&= 0.
\end{aligned} \tag{D.10}$$

This leads to an expression for A_3:

$$A_3 = \frac{\sqrt{\tfrac{3}{2}\,A_1^3\gamma\,\Delta}\,\left(\tfrac{1}{4} - \dfrac{A_1^2\gamma}{8\,D}\right)}{\dfrac{3}{4}A_1^2\gamma + \dfrac{F_1}{A_1} + 4\delta\omega_0 - 8\delta^2} \tag{D.11}$$

where $\Delta = 4F_1 - 3A_1^3\gamma + 4A_1\delta(\delta - 2\omega_0)$, $D = \omega_0^2 - 9(\omega_0 - \delta)^2$. This solution remains convoluted, making direct fitting impractical. To reduce complexity, the equation is truncated to retain only coefficients up to order three.

The resulting expression for A_3 is:

$$A_3 = \frac{A_1^{3/2}\sqrt{\gamma}\sqrt{4F_1 - 3A_1^3\gamma + 4A_1\delta^2 - 8A_1\delta\omega_0}}{4\sqrt{6}\,\delta\left(3\delta - 2\omega_0\right)}. \tag{D.12}$$

This relation eliminates the need to assume $A_1 = A_2$, but it has two drawbacks:

1. It depends on F_1, which is difficult to determine experimentally.
2. Its accuracy is expected to be lower, since the maximum order of A_1 is A_1^3, compared with A_1^4 in the alternative expression.

Consequently, the most suitable relation is considered to be Equation D.6, which will therefore be used for analysis and comparison.